Supplementary Materials

Structural Basis for Integration of GluD Receptors within Synaptic Organizer Complexes

Jonathan Elegheert[1], Wataru Kakegawa[2], Jordan E. Clay[1], Natalie F. Shanks[3], Ester Behiels[1], Keiko Matsuda[2], Kazuhisa Kohda[2], Eriko Miura[2], Maxim Rossmann[4], Nikolaos Mitakidis[1], Junko Motohashi[2], Veronica T. Chang[1], Christian Siebold[1], Ingo H. Greger[4], Terunaga Nakagawa[3,*], Michisuke Yuzaki[2,*,†], A. Radu Aricescu[1,*,†]

[1] Division of Structural Biology, Wellcome Trust Centre for Human Genetics, University of Oxford, Roosevelt Drive, Oxford OX3 7BN, UK.

[2] Department of Physiology, Keio University School of Medicine, 35 Shinanomachi, Shinjuku-ku, Tokyo 160-8582, Japan.

[3] Department of Molecular Physiology and Biophysics, School of Medicine, Vanderbilt University, Nashville, TN 37232-0615, USA.

[4] Neurobiology Division, MRC Laboratory of Molecular Biology, Francis Crick Avenue, Cambridge CB2 0QH, UK.

* Co-senior author

† Corresponding author Email: radu@strubi.ox.ac.uk (A.R.A), myuzaki@a5.keio.jp (M.Y.)

This PDF file includes:

Materials and Methods
Supplementary Text
Figures S1-S22
Table S1
References (1-103)

Materials and Methods

Expression and Purification of soluble Cbln1, β-NRX1, GluD1 and GluD2 Proteins

Constructs of the extracellular human glutamate receptor Delta-2 amino-terminal domain (ATD) (GenBank ID NM_001510; $GluD2_{ATD}$: Asp^{24}-Gly^{440}), mouse glutamate receptor Delta-1 ATD (GenBank ID NM_008166; $GluD1_{ATD}$: Asp^{21}-Gly^{436}), human Cerebellin-1 (GenBank ID NM_004352; $Cbln1_{FL}$: Gln^{22}-Leu^{193}, $Cbln1_{C1q}$: Ser^{59}-Leu^{193}, $Cbln1^{C34S,\ C38S}$: Gln^{22}-Leu^{193} with Cys34Ser and Cys38Ser mutations, $Cbln1^{\Delta VRSG}$; Glu^{24}-Leu^{193} with deletion of Val^{55}-Gly^{58} stretch) and human β-Neurexin-1 (GenBank ID NM_138735; β-NRX1: His^{85}-Val^{265}), fused C-terminally with a hexa-histidine (His6) tag, were cloned into the pHLsec vector (*39*). Proteins were expressed by transient transfection in HEK 293T (in the presence of the class I α-mannosidase inhibitor kifunensine (*40*)) or HEK 293S-GnTI$^{-/-}$ (*41*) cells, using an automated procedure (*42*). Five (HEK 293T) to ten (HEK 293S-GnTI$^{-/-}$) days post-transfection, the conditioned medium was collected and buffer-exchanged using a QuixStand benchtop diafiltration system (GE Healthcare) and proteins were purified by immobilized metal-affinity chromatography (IMAC) using pre-packed Nickel Sepharose columns (GE Healthcare). Proteins were concentrated and further purified by size-exclusion chromatography (SEC; Superdex 200 16/60 column, GE Healthcare) in 10 mM HEPES (4-(2-hydroxyethyl)-1-piperazineethanesulfonic acid) pH 7.50, 150 mM sodium chloride and 3 mM calcium chloride (HBS-C). The β-NRX1(+4)–$Cbln1_{FL}$ complex was formed by co-expression using a 1:1 ratio of plasmid DNA templates, resulting in a molar excess of β-NRX1(+4).

Expression, Solubilisation and Purification of Full-length GluD2

All full-length human glutamate receptor Delta-2 (GenBank ID NM_001510; $GluD2_{FL}$: Asp^{24}-Ile^{1007}) variants were cloned into the pHLsec vector (*39*). Constructs for fluorescence-detection size-exclusion chromatography (FSEC) (*43*) and FSEC-thermostability (FSEC-TS) (*44*) screening were C-terminally tagged with monoVenus (mVenus) (*45*) followed by a 1D4 epitope tag (TETSQVAPA) (*46*), while those for SPR analysis carried a C-terminal Avitag followed by a 1D4 tag. Extensive FSEC-TS screening determined that C-terminal truncation of $GluD2_{FL}$ at Lys^{870} ($GluD2^{D24\text{-}K870}$) led to monodisperse protein preparations of good yield. Decyl maltose neopentyl glycol (DMNG, Anatrace) was the most suitable detergent, and GluD2 stability was

enhanced by the addition of cholesterol hemisuccinate (CHS, Anatrace). Small- and large-scale purification of GluD2 variants was based on established protocols (*47*).

Small-scale expression trials for FSEC screening were performed by transient transfection with polyethylenimine (PEI, Sigma-Aldrich) in adherent HEK 293S-GnTI$^{-/-}$ cell cultures (*39*). After 48 h of expression, cells were suspended and solubilized for 1.5 h at 277 K in binding buffer (10 mM HEPES pH 7.2, 300 mM NaCl, 1% (v/v) mammalian protease inhibitor solution (Sigma-Aldrich)) supplemented with 1.3% (w/v) 20:1 DMNG:CHS. After removal of insoluble material by centrifugation (21,000 g; 15 min) the supernatant was diluted with binding buffer to lower the DMNG concentration to 0.8% (w/v) and incubated for 1.5 h at 277 K with Rho-1D4 beads (monoclonal Rho-1D4 antibody (University of British Columbia) coupled to CNBr-activated sepharose beads (GE Healthcare)). Resin-bound samples were washed with washing buffer (10 mM HEPES pH 7.2, 300 mM NaCl, 0.007% (w/v) 20:1 DMNG:CHS) and GluD2 variants were eluted overnight in washing buffer supplemented with 500 mM TETSQVAPA peptide (Genscript)). Samples were loaded onto a Superose 6 3.2/300 column (GE Healthcare) equilibrated in 10 mM HEPES pH 7.2, 150 mM NaCl, 0.007% (w/v) 20:1 DMNG:CHS and attached to a high-performance liquid chromatography system (HPLCs, Shimadzu).

For SPR analysis, large-scale expression and purification of GluD2 variants was established. HEK 293S-GnTI$^{-/-}$ cells were grown in suspension in supplemented protein expression medium (1% sPEM) (PEM (Invitrogen) supplemented with L-glutamine, non-essential amino-acids (Gibco) and 1% fetal calf serum (Sigma)). Transient transfection (~50% efficiency) at a cell density of 2 x 10^6 cells mL^{-1} was realized by harvesting 1 L of cells (300 g; 7 min), resuspending the cells in 150 mL Freestyle medium (Invitrogen) supplemented with 1.5 mg PEI Max (Polysciences) and 0.5 mg plasmid DNA, and shaking them for 5 h at 310 K, after which the medium was topped up to 1.25 L with 1% sPEM. Cells were harvested (750 g; 4 min) 60 h post-transfection, flash-frozen in liquid N2 and stored at 193 K. GluD2 was purified using Rho-1D4 beads essentially as described above, concentrated to 6 g/L using 100 kDa cut-off membranes (Sartorius) and applied on a Superose 6 Increase 10/300 gel filtration column (GE Healthcare) equilibrated with 10 mM HEPES pH 7.2, 150 mM NaCl, 0.007% (w/v) 20:1 DMNG:CHS.

Gene Splicing and Site-Directed Mutagenesis

A multiple-step overlap-extension PCR (Pyrobest Polymerase, Takara Bio) was used for site-directed mutagenesis, construction of chimeric protein constructs and introduction or deletion of splice inserts (*48*); the resulting PCR products were cloned into the pHLsec-His6 or pHLsec-Avitag3 vectors (*39*).

The following internal primer pair was used for the introduction of human β-NRX1 spliced sequence #4 (SS4; GNNDNERLAIARQRIPYRLGRVVDEWLLDK) into β-NRX1(–4);
FP: 5'-CGCATTCCCTATCGGCTAGGGAGAGTGGTGGACGAATGGCTGCTCGATAA AGGGAGGCAACTGACCATCTTCAACTCAC-3'
RP: 5'-CCCTAGCCGATAGGGAATGCGTTGCCGTGCTATGGCTAACCTCTCATTGT CGTTGTTTCCAGCTGGGTATCTCTCAATGAC-3'

Protein Crystallization

Crystallization trials, using 100 nL protein solution plus 100 nL reservoir solution in sitting drop vapor diffusion format, were set up in 96-well Greiner plates using a Cartesian Technologies robot (*49*). $GluD2_{ATD}$ and $GluD1_{ATD}$ were treated with endoglycosidase F1 (EndoF1; 1:100 w/w) for 12 h at 294 K to trim the N-linked glycans down to one N-acetyl glucosamine (NAG) moiety.

EndoF1-treated human $GluD2_{ATD}$ (Asp^{24}-Gly^{440}) at 8.7 g/L crystallized in 20% (w/v) polyethylene glycol 1000, 0.2 M calcium Acetate, 0.1 M imidazole pH 8.0 and 0.4 M NDSB-221 (non-detergent sulfobetaine 221). Crystals were cryoprotected using reservoir solution containing 30% (v/v) ethylene glycol.

EndoF1-treated mouse $GluD1_{ATD}$ (Asp^{21}-Gly^{436}) at 10.3 g/L crystallized in 0.1 M MES (2-ethanesulfonic acid)/imidazole pH 6.5, 10% (w/v) polyethylene glycol 8000, 20% (w/v) ethylene glycol, 0.02 M 1,6-hexanediol, 0.02 M (*RS*)-1,2-propanediol, 0.02 M 1-butanol, 0.02 M 2-propanol, 0.02 M 1,4-butanediol and 0.02 M 1,3-propanediol. Crystals were cryoprotected using reservoir solution containing 30% (v/v) ethylene glycol.

Human $Cbln1_{C1q}$ (Ser^{59}-Leu^{193}; containing a N-linked oligomannose-type glycan tree at Asn^{79}) was concentrated to 4.8 g/L in the presence of 50 mM L-arginine and L-glutamate and crystallized in 0.2 M sodium malonate pH 7.0, 20% (w/v) polyethylene glycol 3350. Crystals were cryoprotected using reservoir solution containing 30% (v/v) ethylene glycol.

Attempts to crystallise $Cbln1_{FL}$ continuously yielded crystals of only $Cbln1_{C1q}$, indicating cleavage between the N-terminal segment (NTS; Gln^{22}-Ser^{54}) and the C1q-like domain. Cleavage likely occurs at the putative tumor necrosis factor alpha-converting enzyme (TACE) recognition site formed by Ala^{50}-Gly^{58} (ALGIS|VRSG; where "|" denotes the cleavage site; Fig. S4D). Human $Cbln1^{\Delta VRSG}$ (Glu^{24}-Leu^{193}; containing a N-linked oligomannose-type glycan tree at Asn^{79}, but with deleted Val^{55}-Gly^{58} stretch) at 11.9 g/L crystallized in 15% (v/v) glycerol, 8.5% (v/v) isopropanol, 17% (w/v) polyethylene glycol 4000, 0.085 M Na.HEPES pH 7.5 and 0.02 M sodium bromide (crystal form 1). Crystals were cryoprotected using reservoir solution containing 30% (v/v) ethylene glycol. A second crystal form of $Cbln1^{\Delta VRSG}$ at 6.0 g/L was obtained in 2.75 M 1,6-Hexanediol, 50 mM Tris pH 8.0 and 5 mM magnesium sulphate (crystal form 2). Crystals were cryoprotected using reservoir solution.

Human $Cbln1_{C1q\text{-}fused}$–$GluD2_{ATD}$ (containing all N-linked oligomannose-type glycan trees; Fig. S7) was concentrated in the presence of 250 mM NDSB-256 (Affymetrix) to 2.7 g/L and crystallized in 60% (v/v) tacsimate pH 7.0 (Hampton Research; 1.8305 M malonic acid, 0.25 M ammonium citrate tribasic, 0.12 M succinic acid, 0.3 M DL-malic acid, 0.4 M sodium acetate trihydrate, 0.5 M sodium formate, and 0.16 M ammonium tartrate dibasic). Crystals were cryoprotected in 72% (v/v) tacsimate pH 7.0, 10% (v/v) glycerol.

Crystallographic Data Collection and Structure Determination

Diffraction data for $GluD2_{ATD}$ were collected at Diamond Light Source (DLS) I04 to a nominal resolution of 1.75 Å in space group (SG) *I*222. The structure was determined by molecular replacement using the $GluA2_{ATD}$ (PDB code 2WJW) structure (*28*). The $GluD2_{ATD}$ dimer (Fig. S2B) is formed via symmetry operation around the *I*222 unit cell *c* axis.

Diffraction data for $GluD1_{ATD}$ were collected at DLS I04-1 to a nominal resolution of 2.30 Å in SG $P3_221$. The structure was determined by molecular replacement using the refined $GluD2_{ATD}$ structure.

Diffraction data for $Cbln1_{C1q}$ were collected at DLS I04 to a nominal resolution of 2.35 Å in SG *P*6. The structure was determined by molecular replacement using the collagen X NC1 trimer (PDB code 1GR3) structure (*50*). Crystals of $Cbln1_{C1q}$ were pseudomerohedrally twinned, emulating a *P*622 metric symmetry via the twinning operator *h, -h-k, -l*. The $Cbln1_{C1q}$ trimer (Fig.

S4C) is formed by rotation of the Cbln1$_{C1q}$ monomer in the asymmetric unit around the *P*6 unit cell *c* axis.

Diffraction data for Cbln1$^{\Delta VRSG}$ were collected at DLS I03 to a nominal resolution of 2.80 Å in SG *C*222$_1$ (crystal form 1) and 7.00 Å in SG *I*2$_1$3 (crystal form 2). The structure was determined by molecular replacement using the refined Cbln1$_{C1q}$ structure. The Cbln1$^{\Delta VRSG}$ head-to-head dimer-of-trimers (Fig. S9A and S9B) is formed by rotation of the Cbln1$_{C1q}$ trimer in the asymmetric unit around the *C*222$_1$ unit cell *a* axis (crystal form 1) or around the *I*2$_1$3 unit cell *b* axis (crystal form 2).

Diffraction data for the Cbln1$_{C1q\text{-}fused}$–GluD2$_{ATD}$ chimera were collected at DLS I24 to a nominal resolution of 3.10 Å in SG *P*6$_1$22. Due to radiation sensitivity of the crystals, two 30-degree data wedges from separate, isomorphic crystals were combined. The structure was determined by molecular replacement using our refined high-resolution crystal structures of GluD2$_{ATD}$ and Cbln1$_{C1q}$. The full ~400 kDa dimer-of-dimers Cbln1$_{C1q\text{-}fused}$–GluD2$_{ATD}$ complex is generated via symmetry operation around the *P*6$_1$22 unit cell *a* and *b* axes.

All data were indexed, integrated, and scaled using the automated XIA2 expert system (*51*), using the Labelit (*52*), Pointless and Aimless (*53, 54*), and XDS (*55*) programs. Crystallographic data collection and refinement statistics are presented in Table S1. All molecular replacement was performed using the program Phaser (*56*).

Cbln1$^{\Delta VRSG}$ crystal form 1 crystals diffracted anisotropically to ~3.8 Å along the *k* axis; ellipsoidal truncation and anisotropic scaling of diffraction data was performed using the Diffraction Anisotropy Server (*57*); overall data completeness in the 3.8-2.8 Å resolution bin after ellipsoidal truncation is 55% (Table S1).

Crystallographic Refinement and Model Analysis

Maximum-likelihood refinement and automated model building of GluD2$_{ATD}$, GluD1$_{ATD}$, Cbln1$_{C1q}$ and Cbln1$^{\Delta VRSG}$ (crystal form 1) was performed with PHENIX (*58*), using automated X-ray and atomic displacement parameter (ADP) weight optimisation, and torsion angle non-crystallographic symmetry (NCS) restraints where applicable. In the case of Cbln1$_{C1q}$, the twinning operator (*h, -h-k, -l*) was applied, and the twinning fraction refined, in final rounds of least-squares refinement. Rigid body refinement of Cbln1$^{\Delta VRSG}$ (crystal form 2) was performed with PHENIX (*58*) using global NCS restraints. Refinement of the Cbln1$_{C1q\text{-}fused}$–GluD2$_{ATD}$

chimera was performed with Refmac using "jelly body" restraints (*59, 60*), Buster (*61*) and finally PHENIX (*58*). Torsion angle NCS restraints, high-resolution reference structure restraints, and automated X-ray and ADP weight optimisation were applied throughout. All manual model building was performed using Coot (*62*). Structure validation was performed with PHENIX using MolProbity routines (*58, 63*).

Interface analysis was performed using PISA (*64*) as implemented in Coot (*62*), and using the program Intervor (*65*). Molecular representations were made using the program PyMol (*66*). Analysis of protein hydrophobicity was based on the Eisenberg hydrophobicity scale (*67*). Calculation of pairwise root-mean-square deviations (r.m.s.d.) between structural model coordinates was performed using the program PyMol (*66*). Structural alignment of the iGluR ATDs was performed using the program SHP (*68*), and alignments were annotated to primary protein sequences using the program ALINE (*69*).

Owing to the availability of high-resolution structures of subcomponents and high crystal solvent content (70%), the $Cbln1_{C1q\text{-}fused}$–$GluD2_{ATD}$ complex electron density map was very clear and allowed tracing of the complete $Cbln1_{C1q}$ and $GluD2_{ATD}$ chains and confident positional refinement of nearly all amino acid side chains (Fig. S8D). The linkers interconnecting the C1q monomers and the long $(G_2S)_{10}$ linker were not visible in the electron density, suggesting that they are disordered and do not interfere with formation of the native interface or impose a certain orientation.

Sequence Alignments and Conservation Analysis

Mining of protein sequence databases was performed using the Delta-Blast program (*70*). Sequence lists were manually curated and sequences were aligned using the program MUSCLE (*71*). Sequence conservation scores for individual residue positions of GluD1 and -2 (205 total sequences) and Cbln1, -2, -3, and -4 (330 total sequences) homologs were assigned to $GluD2_{ATD}$ and $Cbln1_{C1q}$ structural templates, respectively, using the ConSurf web server (*72*). Sequence alignments were visualized using the program ALINE (*69*).

Single Particle Negative-Stain Electron Microscopy (EM)

Cbln1, the β-NRX1(+4)–Cbln1 complex and the $Cbln1_{C1q\text{-}fused}$–$GluD2_{ATD}$ chimera were adsorbed to glow-discharged grids and negatively stained with 0.7% uranyl formate as previously

described (*73*). Images were recorded using a FEI Sphera or FEI TF20 electron microscope operated at an acceleration voltage of 200 keV, magnification of 50,000 × and defocus values ranging form –1.5 to –1.6 μm. All images were recorded using SO-163 films (Kodak) and developed with a Kodak D-19 developer at full strength for 12 min at 293 K. The electron micrographs were digitized with a CoolScan 9000 (Nikon) using a 6.35 μm step size, and the pixels were binned by a factor of three. As a result, the pixel size at the specimen level was 3.8 Å.

In order to generate projection averages for Cbln1 and the β-NRX1(+4)–Cbln1 complex, particles were interactively selected using the WEB display program in SPIDER (*74*). Using SPIDER, projection averages were calculated from windowed images over 8 cycles of K-means classification and multi-reference alignment specifying 100 classes. Representative images of raw particles were recorded on a CCD camera (Gatan, Ultrascan).

Multi-angle Light Scattering (MALS)

Protein samples concentrated to ~1.0 g/L were injected into an HPLC-driven SEC column (Superdex 200 10/30 column, GE Healthcare) equilibrated with HBS buffer. The SEC column was coupled to an online UV detector (Shimadzu), an 18-angle light scattering detector (DAWN HELEOS), and a refractive index detector (Optilab T-rEX) (Wyatt Technology). Proteins for MALS contained N-linked oligomannose-type sugars, and molecular mass determination was performed using an adapted RI increment value (*dn*/*dc* standard value; 0.185 mL/g) to account for the glycosylation state. Data analysis was carried out using the ASTRA V software (Wyatt Technology).

Isothermal Titration Calorimetry (ITC)

Calorimetric measurements were carried out using samples purified by SEC in HBS buffer. Experiments were carried out using a VP-ITC MicroCalorimeter (GE Healthcare) at 310 K, and data were analyzed using the Origin ITC analysis software package. Titrations were always preceded by an initial injection of 3 μL and were carried out using sequential 10 μL injections with continuous stirring. The data were fitted to the "one binding site model", and apparent molar reaction enthalpy (ΔH°), apparent entropy (ΔS°), association constant (K_A), and binding stoichiometry (N) was determined.

Surface Plasmon Resonance (SPR)

cDNA for the soluble GluD and Cbln protein variants was cloned into the pHLsec-Avitag3 vector (*39*), resulting in proteins carrying a C-terminal biotin ligase (BirA) recognition sequence (Avitag). Constructs were co-transfected with pDisplay-BirA-ER (Addgene plasmid 20856; coding for an ER-resident biotin ligase) (*75*) in HEK 293T cells in small-scale 6- or 12-well plates in a 3:1 pHLsec:pDisplay stoichiometric ratio for *in vivo* biotinylation. A final concentration of 100 µM D-biotin was maintained in the expression medium to ensure near-complete biotinylation of the recognition sequence. After 48 h of expression, conditioned medium was collected and dialysed against 10 mM HEPES pH 7.4, 150 mM sodium chloride, 3mM calcium chloride and 0.005% (v/v) Tween-20 (HBS-CT). SPR experiments were performed on a Biacore T200 machine (GE Healthcare) operated at a data collection frequency of 10 Hz; *i.e.* a temporal resolution of 0.1 sec. Streptavidin (Sigma-Aldrich) was chemically coupled via amine coupling chemistry onto CM5 chips to a response unit (RU) level of 5000 RU. Then, biotinylated proteins were captured to the desired RU level. In each instance, for every two analyte binding cycles, a buffer injection was performed, allowing for double referencing of the binding responses (*76*).

For the interaction of $GluD2_{ATD}$-F76D and $GluD1_{ATD}$-F73D with $Cbln1_{C1q}$ (Fig. S6D and S6E, respectively), $Cbln1_{C1q}$ was coupled to 1200 RU to achieve maximal $GluD_{ATD}$ binding responses of 150 RU. SPR running buffer composition was HBS-CT, supplemented with 1.0 g/L bovine serum albumin (BSA) (yielding HBS-CTB buffer) as passivating agent to prevent binding to the carboxymethyldextran-based SPR chips. BSA was added to the concentrated $GluD2_{ATD}$-F76D and $GluD1_{ATD}$-F73D stock solutions to a final concentration of 1.0 g/L. Injection of 10 concentrations of $GluD2_{ATD}$-F76D and $GluD1_{ATD}$-F73D prepared in a twofold dilution series from a 40 µM and 20 µM stock concentration, respectively, was performed in order of increasing concentration. Each sample was injected for 60 sec at a flow rate of 50 µL/min, followed by a 120 sec dissociation phase. The binding data were processed using Scrubber 2.0 (BioLogic Software) and fitted to a 1:1 Langmuir kinetics binding model without mass transfer to determine k_{on} and k_{off}, and K_D ($K_D = k_{off}/k_{on}$). Fast dissociation kinetics ($k_{off} \geq 0.5$ sec^{-1}) prevented accurate K_D determination. No saturation of binding was observed with analyte concentrations beyond 100 µM, also preventing K_D determination via equilibrium analysis.

For the interaction of $GluD2_{ATD}$ interface mutants with $Cbln1_{FL}$ (Fig. S15A, S16B and S17A), mutations were introduced on the $GluD2_{ATD}$-F76D backbone; this orientation allowed efficient screening of small-scale produced mutants and the avidity inherent to this experimental setup was exploited to achieve stronger signal. $GluD2_{ATD}$-F76D variants were coupled to 1000 RU. SPR running buffer composition was HBS-CT. Injection of 12-18 concentrations of $Cbln1_{FL}$, prepared in a twofold dilution series from a 100 µM stock concentration, was performed in order of increasing concentration. Each sample was injected for 200 sec at a flow rate of 10 µL/min, followed by a 600 sec dissociation phase. For the GluD2 mutants eliciting increased avidity (E343A, K346A, S349A and M350A), surfaces were regenerated using successive 30 sec injections of 10 mM HEPES pH 7.5, 1.0% (w/v) CHAPS (3-[(3-Cholamidopropyl)dimethylammonio]-1-propanesulfonate). Equilibrium binding analysis was performed using Scrubber 2.0 (BioLogic Software) and data was fitted to a "two-site" binding model in Prism 6 (Graphpad). However, since accurate K_D determination is not possible from this setup due to the avidity, we judged the impact of the Ala-mutations based on increase or decrease of the absolute binding response levels, relative to the control ($GluD2_{ATD}$-F76D; "Ref").

For the interaction of $GluD2_{ATD}$ with $Cbln1_{FL}$, $Cbln1^{C34S,\ C38S}$, $Cbln1_{C1q}$ and the corresponding Y122A-R124A-D147A triple mutants (Fig. S5C and S16A), Cbln1 variants were coupled to 500 RU. SPR running buffer composition was HBS-CTB. BSA was added to the concentrated $GluD2_{ATD}$ stock solutions to a final concentration of 1.0 g/L. Injection of 12 concentrations of $GluD2_{ATD}$, prepared in a twofold dilution series from a 100 µM stock concentration, was performed in order of increasing concentration. Each sample was injected for 150 sec at a flow rate of 25 µL/min, followed by a 120 sec dissociation phase.

For the interaction of the combined E343A, K346A, S349A, M350A $GluD2_{ATD}$ interface mutant with $Cbln1_{FL}$ (Fig. S17B), mutations were introduced on the $GluD2_{ATD}$-F76D backbone. $GluD2_{ATD}$-F76D served as wild-type interface control. The combined D24A, I26A, E61A, R345A $GluD2_{ATD}$ interface mutant (introduced on the $GluD2_{ATD}$-F76D backbone) was immobilized in the reference channel. SPR running buffer composition was HBS-CT. Injection of 5 concentrations of $Cbln1_{FL}$, prepared in a twofold dilution series from a 10 µM stock concentration, was performed in order of increasing concentration. Each sample was injected for 120 sec at a flow rate of 10 µL/min, followed by an intermittent 120 sec dissociation phase or a final 600 sec dissociation phase.

For the interaction of $GluD2_{FL}$ containing the C-terminal truncation at Lys^{870} ($GluD2^{D24\text{-}K870}$) with β-NRX1(+4)–$Cbln1_{FL}$ (Fig. S5A), a C-terminal biotin ligase (BirA) recognition sequence (Avitag) was added to the construct. $GluD2^{D24\text{-}K870}$ was biotinylated *in vitro* using recombinant BirA. $GluD2^{D24\text{-}K870}$ was coupled to 900 RU to achieve maximal $Cbln1_{FL}$ binding responses of 100 RU. $GluD2^{\Delta ATD}$ containing the C-terminal truncation at Lys870 ($GluD2^{\Delta ATD,\ V441\text{-}K870}$) was coupled to 600 RU in the reference channel. Running buffer was 10 mM HEPES pH 7.2, 150 mM NaCl, 3 mM $CaCl_2$, 0.007% (w/v) 20:1 DMNG:CHS. Injection of 5 concentrations of β-NRX1(+4)–$Cbln1_{FL}$, prepared in a twofold dilution series from a 625 nM stock concentration, was performed in order of increasing concentration. Each sample was injected for 120 sec at a flow rate of 25 µL/min, followed by an intermittent 120 sec dissociation phase or a final 600 sec dissociation phase. The binding data were processed using BiaEvaluation software (GE Healthcare) and fitted to a two-state single-cycle kinetics (SCK) binding model without mass transfer to determine $k_{on,1}$, $k_{on,2}$, $k_{off,1}$ and $k_{off,2}$, and apparent K_D ($K_{D,app}$). $GluD2^{D24\text{-}K870}$ was coupled to 3500 RU in the experiment that gauged how omission of $CaCl_2$ reduced the active GluD2 surface population (Fig. S11B). Injection of 5 concentrations of β-NRX1(+4)–$Cbln1_{FL}$, prepared in a twofold dilution series from a 10 µM stock concentration, was performed in order of increasing concentration.

Fluorescence-Detected Sedimentation Analytical Ultracentrifugation (FDS-AUC)

N-terminal labeling of $GluD2_{ATD}$ was performed by incubation with 30-fold excess of 5(6)-carboxyfluorescein succinimidyl ester (FAM; Biotium) at 293 K in the dark for 30 min. The reaction was quenched with excess primary amine (1 M Tris-HCl pH 7.0). Excess label was removed by dialysis, and labeled protein was re-purified by SEC. Labeling efficiency was estimated spectrophotometrically to be 1.2:1 fluorophore:protein. Samples were prepared by dilution of concentrated protein stock with AUC buffer (50 mM sodium phosphate pH 7.4, 150 mM sodium chloride, and 0.2 g/L BSA).

FDS-AUC with fluorescence detection was performed using an Optima XL-I analytical ultracentrifuge (Beckman Coulter) equipped with a fluorescence detection system (Aviv Biomedical). $GluD2_{ATD}$, in a concentration range of 1.5 to 636 nM, was loaded in cell assemblies with standard 12 mm Epon double-sector centerpieces installed in a Ti-60 rotor. FDS-AUC sedimentation experiments were performed at 50,000 rpm at 283 K after a 3 h equilibration step

at 283 K. A total of 400 scans were acquired in intervals of 2.5 min. Concentration gradients were fit with sedimentation coefficient distributions (c(s)) using the program SEDFIT (*77*). Subsequent fitting of sedimentation profiles to normal distributions and K_D calculations were done with the pro Fit software (QuantumSoft); c(s) distributions were deconvoluted into monomeric and dimeric fractions and separately integrated to determine the K_D of dimer formation ($K_{D,dimer}$).

Absorbance Detection Analytical Ultracentrifugation

$GluD2_{ATD}$-F76D, in a concentration range of 0.4 to 100 μM, was subjected to analytical sedimentation velocity ultracentrifugation (SV-AUC) with far UV absorbance detection. SV-AUC was performed in an Optima XL-1 analytical centrifuge at 40,000 rpm at 283 K after a 3 h equilibration step at 283 K. No dimeric ATD species could be observed.

HEK 293–Cerebellar Granule Cell (GC) Hemi-synapse Formation Assay

Mixed cerebellar cultures were prepared from embryonic day 17 to day-of-birth mice, as described previously (*16*). Cells were plated at a density of 2.5×10^5 on plastic coverslips (13.5 mm diameter) and were maintained in DMEM-F12 medium containing 100 μM putrescine, 30 nM sodium selenite, 0.5 ng/mL tri-iodothyronine, 0.25 g/L BSA, 3.9 mM glutamate and N3 supplement (100 μg/mL apo-transferrin, 10 μg/mL insulin and 20 nM progesterone) in 5% CO_2 at 310 K.

Heterologous synapse formation assays using HEK 293T cells were performed as described previously (*78*). Briefly, HEK 293T cells transfected with $GluD2^{WT}$, $GluD2^{D24A,\ I26A,\ E61A,\ R345A}$, $GluD2^{E343A,\ K346A,\ S349A,\ M350A}$, $GluD2^{F76D}$, $GluD2^{ATD\text{-}LBD\_GLYCAN\_WEDGE}$ and $GluD2^{\Delta ATD}$ were added to the primary cultured neurons at 8 days *in vitro* (DIV) and co-cultured for 2 d in the presence of 10 μM 5-fluoro-2-deoxyuridine. Cells in dissociated cultures were fixed with PBS containing 4% (v/v) PFA for 20 min on ice, followed by 100% methanol at 253 K for 10 min. After permeabilization with 0.4% Triton X-100 in PBS containing 2% (w/v) BSA and 2% (v/v) normal goat serum for 1 h at 293 K, the cells were treated with rabbit anti-GluD2 (1:1000, (*79*)) and mouse anti-synaptophysin (1:500, Sigma-Aldrich) primary antibodies, followed by goat anti-rabbit secondary antibodies (1:1000) conjugated to Alexa Fluor 488, and goat anti-mouse secondary antibodies (1:1000) conjugated to Alexa Fluor 546.

Fluorescence images were captured using an upright microscope (BX63; Olympus). To quantify the accumulation of synaptophysin in the transfected HEK 293 cells, images were randomly captured using fixed gains and exposures for each fluorescent channel. Three independent experiments were performed, and 10-13 fields were evaluated per experiment, for a total of n = 34-37 fields. Each field covered a 665 × 665 μm^2 surface area and contained a minimum of 15 transfected HEK cells. The images were analysed using ImageJ. GluD2-immunopositive cells dropped onto neurons were selected as regions of interest (ROIs). The intensity of the synaptophysin immunoreactivity within the segmented area was averaged, and the background synaptophysin immunoreactivity within the non-segmented area was subtracted.

Recombinant Sindbis Virus Production and Infection

The recombinant Sindbis virus for the expression of $GluD2^{WT}$, $GluD2^{D24A,\ I26A,\ E61A,\ R345A}$, $GluD2^{E343A,\ K346A,\ S349A,\ M350A}$, $GluD2^{F76D}$ and $GluD2^{ATD\text{-}LBD\_GLYCAN\_WEDGE}$ in combination with a GFP was constructed as previously described (*80*). Briefly, under deep anesthesia, with an intraperitoneal injection of ketamine/xylazine (80/20 mg/kg; Sigma-Aldrich), 2 μL of the solution containing the recombinant Sindbis virus (titer; 1.0 × $10^{8\text{-}9}$ TU/mL) was injected into the subarachnoidal space above the cerebellar vermis in immature (P11-P17) or mature (> P30) *Grid2*-null mice at a rate of 40 μL/h (*78*). In some experiments for electron microscopy and electrophysiology, the viral solution was directly injected into the vermis of cerebellar lobules V-VIII using a glass pipette (30 μm in diameter) and a microinjector (Nanoliter; World Precision Instruments). One day after infection, the mice were used for each experiment.

Immunohistochemistry and Pre- and Post-embedding Immunogold EM Analysis

Under deep anesthesia using a pentobarbital, virus-infected mice were fixed by cardiac perfusion with 0.1 M phosphate buffer (PB; pH 7.4) containing 4% (v/v) paraformaldehyde (PFA); the brain was then removed and the cerebellum was further immersed in the same fixative for 2 h. Parasagittal slices (300 μm thickness) were prepared using a DTK-2000 microslicer (D.S.K.).

To identify the Sindbis virus infected Purkinje cells (PCs); virally expressed GFP was labeled by the silver-enhanced pre-embedding immunogold method using rabbit anti-GFP antibody (1:200, Frontier Institute), 1.4 nm gold particle-conjugated anti-rabbit antibody

(Nanogold, Nanoprobes Inc.), and a silver enhancement kit (HQ silver, Nanoprobes Inc. or R-Gent SE-EM, Aurion).

To evaluate synaptic location of virally transfected GluD2^{WT}, GluD2$^{D24A,\ I26A,\ E61A,\ R345A}$, GluD2$^{E343A,\ K346A,\ S349A,\ M350A}$, GluD2^{F76D} and GluD2$^{ATD\text{-}LBD_GLYCAN_WEDGE}$, the double post-embedding immunogold method was performed (*81*). Parasagittal slices (300 μm thickness) were cryoprotected with 30% sucrose in PB and rapidly cryo-fixated with liquid propane (EM CPC unit, Leica). Frozen sections were immersed in 0.5% uranyl acetate in methanol at 183 K in a freeze-substitution unit (EM AFS, Leica), infiltrated at 228 K with Lowicryl HM-20 resin, and polymerized with UV light. After etching with a saturated solution of NaOH in absolute ethanol for 3 sec, sections on nickel grids were blocked with 2% (w/v) BSA in 10 mM Tris-buffered saline (TBS) pH 7.6 containing 0.05% (v/v) Tween-20 (TBS-T). Then, the sections were immunoreacted with rabbit anti-GFP antibody (1:200, Frontier Institute) overnight, and then with 20 nm colloidal gold-conjugated anti-rabbit antibody (1:100; British Bio Cell International) in TBS-T for 1 h. Afterwards, grids were blocked with 2% (v/v) normal rabbit serum and again immunoreacted for 4 h with guinea pig anti-GluD2 antibody and for 1 h with 10 nm colloidal gold-conjugated anti-guinea pig antibody. Grids were then stained with 2% uranyl acetate for 5 min and with mixed lead solution for 30 sec.

Electron micrographs were taken randomly by a JEM-1230 or JEM-1400Plus electron microscope (JEOL). For quantitative analysis, the numbers of contacted PF-PC synapses expressing GFP and immunogold particles were counted on electron micrographs.

Electrophysiology on Mouse Cerebellar Slices

Parasagittal cerebellar slices (200 μm thickness) were prepared 24 h after virus injection as previously described (*8, 82*), from immature (P11-P17) wild-type, *Cbln1*-null and *Grid2*-null mice, from mature (> P30) *Cbln1*-null mice, and from immature (P11-P17) *Grid2*-null mice expressing GluD2^{WT}, GluD2$^{D24A,\ I26A,\ E61A,\ R345A}$, GluD2$^{E343A,\ K346A,\ S349A,\ M350A}$, GluD2^{F76D} or GluD2$^{ATD\text{-}LBD_GLYCAN_WEDGE}$. Whole-cell patch clamp recordings were made from GFP-expressing PCs using a 60 × water-immersion objective attached to an upright microscope (BX51WI; Olympus) at 293 K. The resistance of patch pipettes was 3-5 MΩ when filled with an intracellular solution of following composition: 65 mM Cs-methanesulfonate, 65 mM K-gluconate, 20 mM HEPES, 10 mM potassium chloride, 1 mM magnesium chloride, 4 mM

adenosine 5'-triphosphate disodium salt hydrate (Na_2ATP), 1 mM guanosine 5'-triphosphate sodium salt hydrate (Na_2GTP), 5 mM sucrose and 0.4 mM EGTA pH 7.25 (295 mOsm/kg). The solution used for slice storage and recording consisted of the following: 125 mM sodium chloride, 2.5 mM potassium chloride, 2 mM calcium chloride, 1 mM magnesium chloride, 1.25 mM monosodium phosphate (NaH_2PO_4), 26 mM sodium bicarbonate ($NaHCO_3$), and 10 mM D-glucose; bubbled continuously with 95% O_2 and 5% CO_2. Picrotoxin (100 μM, Sigma-Aldrich) was always added to the saline solution to block inhibitory synaptic transmission.

Endogenous D-Ser is released at PF-PC synapses from neighboring Bergman glia by burst stimulation (BS) of PFs in immature cerebellar slices (*8*). D-Ser degrading enzyme, D-amino acid oxidase (DAAO), is not expressed in cerebellar tissues during the first postnatal month (*8, 83*).

PF-evoked excitatory postsynaptic currents (PF-EPSCs) were recorded successively at a frequency of 0.1 Hz from PCs clamped at –80 mV. Long-term depression (LTD) was recorded from parasagittal slices 24 h after virus injection. After stable PF-EPSCs were observed for at least 10 min, cerebellar LTD was induced by applying a burst PF stimulation (BS) combined with direct PC depolarization (ΔV) (BS/ΔV; 30 trials of [10 × PF stimuli at 50 Hz together with 500-msec PC depolarizing pulses from a holding potential of –60 to +20 mV] at 1 Hz), in immature cerebellar slices. In all LTD recordings, NMDA receptor inhibitors (100 μM D-AP5 and 25 μM MK801) were constantly applied to the saline solution (*8*). In some experiments, D-serine (200 μM for 10 min) was applied to the extracellular solution of the cerebellar slices. Access resistances were monitored every 10 sec by measuring the peak currents in response to 2 mV, 50-msec hyperpolarizing steps throughout the experiments; the measurements were discarded if the resistance changed by more than 20% of its original value. Current responses were recorded using an Axopatch 200B amplifier (Molecular Devices), and the pClamp software (version 9.2; Molecular Devices) was used for data acquisition and analysis. The signals were filtered at 1 kHz and digitized at 4 kHz.

Electrophysiology of HEK 293 Cells Expressing GluD2 Lurcher (Lc) Variants

$GluD2^{WT}$ *Lurcher* ($GluD2^{WT/Lc}$), and $GluD2^{ATD\text{-}LBD\_GLYCAN\_WEDGE}$ *Lurcher* ($GluD2^{GW/Lc}$) were introduced into HEK 293T cells using the pTracer-EGFP plasmid; a double-cistron expression vector that also encodes enhanced GFP (EGFP) (*84*). Electrophysiological recordings were performed as previously described (*84*). HEK 293T cells expressing $GluD2^{WT/Lc}$ or $GluD2^{GW/Lc}$

were perfused in an extracellular solution containing 150 mM NaCl, 5 mM KCl, 0.5 mM $CaCl_2$, 1.5 mM $MgCl_2$, 20 mM HEPES pH 7.3 and 20 mM D-glucose. Transfected cells were identified through their expression of EGFP under an inverted microscope (Diaphot TMD, Nikon) and whole-cell patch-clamp recordings were made using an Axopatch 200B (Axon Instruments) at 293 K. Patch pipettes had a resistance of 4-6 MΩ when filled with following intracellular solution: 150 mM CsCl, 1 mM $MgCl_2$, 10 mM HEPES pH 7.3, 10 mM EGTA and 10 μM spermine (Sigma-Aldrich) to sustain rectification of lurcher currents.

To measure lurcher-current modulation by D-serine, HEK 293T cells were serially exposed to the extracellular solutions containing D-serine ranging from 10 μM to 3 mM. Voltage ramps from –80 to +60 mV were applied to obtain current-voltage (*I-V*) relationships after 2.5 min incubation with the D-serine-containing solutions. At the end of each experiment, the extracellular solution was switched to an *N*-methyl-D-glucamine (NMDG) solution consisting of 150 mM NMDG, 5 mM KCl, and 20 mM HEPES pH 7.3, and a voltage ramp was applied to measure background leak currents of HEK 293T cells. Data were digitized at 10 kHz with a 2 kHz low-pass filter. The liquid junction potential was corrected upon data collection. The currents measured in regular extracellular solutions subtracted by those of the NMDG solution were regarded as the lurcher currents. Inhibition effect of D-serine was calculated by the following equation;

$$\% \text{ Inhibition} = (I_{0@-60mV} - I_{D\text{-serine}@-60mV} / I_{0@-60mV}) \times 100$$

where $I_{0@-60mV}$ or $I_{D\text{-serine}@-60mV}$ designate the lurcher currents at –60 mV in a D-serine-free or in a D-serine-containing solution, respectively. Dose-inhibition curves for $GluD2^{WT/Lc}$ and $GluD2^{GW/Lc}$ were obtained by sigmoidal curve fitting using Hill's equation and the IC_{50} values were derived.

Mouse Behavioural Analysis

To examine gross sensorimotor coordination in the virus-infected immature (P11–P17) *Grid2*-null mice, the accelerated rotor-rod test was performed as previously described (*8*). This paradigm was chosen because conventional cerebellum-dependent learning tasks, such as the eye blink-conditioning test, cannot be used in immature mice. Briefly, *Grid2*-null mice virally expressing $GluD2^{WT}$, $GluD2^{D24A,\ I26A,\ E61A,\ R345A}$, $GluD2^{E343A,\ K346A,\ S349A,\ M350A}$, $GluD2^{F76D}$ or

GluD2$^{ATD\text{-}LBD_GLYCAN_WEDGE}$ were, one day after virus injection, placed on a rotating rod that accelerated from 4 to 40 rotations per minute (rpm) in 5 min. The retention time of each mouse was then measured. Five successive sessions were performed with a 30 min interval, and each session consisted of five trials with a 30 sec interval.

Data Analysis and Statistics

Data are presented as means ± SEM. Statistical analyses were performed using the Excel statistics 2012 add-in software (Social Survey Research Information Co.) and significant differences were defined as $*p < 0.05$, $**p < 0.01$, $***p < 0.001$, and $****p < 0.0001$. For comparison between multiple groups, we used a Mann-Whitney *U* test or Tukey's test. For multiple comparisons with a control group, we used a Kruskal-Wallis test followed by a Steel-Dwass *post-hoc* test. When multiple comparisons were performed between two groups in various time points, we used a two-way ANOVA followed by a Bonferroni *post-hoc* test.

Animal Care and Treatment

All procedures related to animal care and treatment were approved by the Animal Resource Committee of the Keio University School of Medicine.

Supplementary Text

Structure of the GluD2 and GluD1 Amino-terminal Domains

We solved the crystal structure of the GluD2 ATD at 1.75 Å (Fig. S1, S2 and Table S1). $GluD2_{ATD}$ adopts a bi-lobed clamshell-like architecture like all other iGluR ATDs, containing an upper lobe R1 and lower lobe R2; extensive R1-R1* and R2-R2* (an asterisk denotes components from the second ATD monomer) dimer contacts are formed by juxtaposed α-helices 2 and 3 (994 $Å^2$ buried surface area (BSA)), and α-helix 5 and β-strand 7 (620 $Å^2$ BSA), respectively (Fig. S2B).

In NMDA receptors, binding of allosteric modulators at the ATD alters agonist potency at the LBD (*85-87*). It is currently unclear whether ATDs in the AMPA, Kainate or Delta subfamilies have a similar ability to bind small-molecule ligands that could potentially function as allosteric modulators. Surprisingly, the cleft formed between lobes R1 and R2 in $GluD2_{ATD}$ is, in contrast to all the GluA/K/N ATDs, occupied by a long loop protruding from lobe R1 (Fig. S2C). The twelve amino acid stretch connecting Arg^{121} and Gly^{132}, which we term the "cleft loop", connects β-strands 4 and 5 and provides a 862 $Å^2$ contact surface that forms a structural bridge between R1 and R2 (Fig. S2D). Residues Ser^{122}, Thr^{123}, Gly^{125}, Thr^{126}, Ser^{129} and Gly^{130} contact R2 through an extensive hydrogen-bonding network involving numerous water molecules. Arg^{121} and Arg^{128} form bifurcated salt-bridges with Glu^{321} and Glu^{263}, respectively. In addition, the GluD-specific Cys^{99}-Cys^{131} disulfide bridge, located at the outer rim of the R1-R2 cleft, further stabilizes the cleft loop conformation (Fig. S2D).

A different, 32-residue loop structure spanning Pro^{286}-Gln^{317}, which we term the "wing loop", connects R1 and R2 between β-strand 10 and α-helix 9, a site occupied by α-helix 8 in GluA/K ATDs. This loop bears an N-linked glycan on Asn^{293}, is stabilized by a GluD-specific disulfide bond between Cys^{294} and Cys^{306} and partially collapses onto R1 α-helices 1 and 9 (Fig. S2B).

The α-helix 6' (Ile^{217}-Leu^{227}), inserted between R2 lobe α-helix 6 and β-strand 8, is unique to GluD and located at the membrane-proximal end of the ATD, extending towards the LBD layer, thus possibly providing contacts between these domains (Fig. S2E).

A crystal structure of the mouse GluD1 ATD at 2.30 Å confirms that the unusual GluD2 ATD cleft loop, wing loop and α-helix 6' features extend across both GluD family members (Cα-

atom r.m.s.d. between $GluD2_{ATD}$ and $GluD1_{ATD}$ dimers is 1.9 Å over 713 positions) (Fig. S2B and Table S1).

Structure of Cbln1

Full-length Cbln1 ($Cbln1_{FL}$) is composed of (i) an N-terminal segment (NTS; Gln^{22}-Ser^{54}) containing two Cysteine residues (Cys^{34} and Cys^{38}), (ii) a short linker predicted to be disordered (Val^{55}-Ala^{60}) and (iii) a putative globular C1q-like domain (Lys^{61}-Leu^{193}) (Fig. S3 and S4A).

We determined the crystal structure of the human Cbln1 C1q-like domain at 2.35 Å ($Cbln1_{C1q}$; Fig. S4C and Table S1). This revealed a canonical nine-stranded β-sandwich jelly-roll topology (AA'B'CDEFGH) similar to the complement factor C1q (PDB 1PK6; Cα-atom r.m.s.d. of 1.0 Å over 91 positions), and a three-fold symmetric trimeric assembly. A structurally distinguishing feature of $Cbln1_{C1q}$ is the insertion of a small α-helix A (αA; Glu^{76}-Thr^{81}), containing an N-linked glycan at Asn^{79}, between β-strands A and A' (Fig. S3 and S4C).

The Cbln1 cysteine-rich NTS serves to link individual $Cbln1_{C1q}$ trimers into a higher order oligomer (*26*). Molecular mass determination using MALS confirmed that $Cbln1_{C1q}$ is trimeric (59.8 ± 1.0 kDa), and $Cbln1_{FL}$ is hexameric (134.0 ± 0.2 kDa) with no evidence for higher order assemblies (Fig. S4B). Mutating Cys^{34} and Cys^{38} in $Cbln1_{FL}$ to Ser to yield $Cbln1^{C34S, C38S}$ (Fig. S4A), prevented hexamer formation (74.7 ± 0.5 kDa) (Fig. S4B).

Cbln1 is proteolysed *in vivo*, a process that separates the NTS from the C1q domain (*26*). Cleavage likely occurs at the putative tumor necrosis factor alpha-converting enzyme (TACE) recognition site formed by Ala^{50}-Gly^{58} (ALGIS|VRSG; where "|" denotes the cleavage site) (Fig. S3 and S4D). Deletion of Val^{55}-Gly^{58} allowed us to crystallize a Cbln1 variant ($Cbln1^{\Delta VRSG}$) containing the NTS and determine its structure at 2.80 Å (Fig. S4E, S9A and Table S1; crystal form 1) and at 7.00 Å (Fig. S9B and Table S1; crystal form 2). In the crystal, two $Cbln1_{C1q}$ trimers form a "head-to-head" arrangement, consistent with a hexameric structure. The distance between the calculated centers of mass of both trimers is 77 Å (Fig. S9A; crystal form 1) and 79 Å (crystal form 2). There was no interpretable electron density near the clustered $Cbln1_{C1q}$ N-termini, suggestive of conformational variability. Thus, the Val^{55}-Ala^{60} linkers likely function as "molecular hinges", connecting the NTS with the C1q domains.

Structural Determinants of the β-NRX1–Cbln1 Binary Complex

We determined which parts of Cbln1 and β-NRX1 are minimally required for binding, as well as their stoichiometry and interaction strength. We measured, using isothermal titration calorimetry (ITC), the interaction between hexameric $Cbln1_{FL}$ and monomeric β-NRX1(+4); it is high-affinity (K_D = 43.5 ± 4.4 nM) and strongly exothermic (ΔH = –31.13 ± 0.25 kcal mol^{-1}) (Fig. S12A). Unexpectedly, one $Cbln1_{FL}$ hexamer binds only one β-NRX1 monomer (1-to-1 binding stoichiometry *N*), breaking the two-fold Cbln1 symmetry (Fig. S12A). $Cbln1^{C34S,\ C38S}$ and $Cbln1_{C1q}$, which both lack the CRR, failed to interact with β-NRX1(+4), and β-NRX1 lacking spliced sequence #4 (SS4; β-NRX1(−4)) did not bind $Cbln1_{FL}$ either (Fig. S12A). These results confirm that the β-NRX1–Cbln1 interaction depends on the presence of β-NRX1 SS4 (*18, 88*), but show that the Cbln1 CRR, and not its globular C1q domain, constitutes the β-NRX1(+4) binding platform.

Using MALS, we confirmed that the mass of the β-NRX1(+4)–$Cbln1_{FL}$ complex (164.5 ± 2.3 kDa) closely matches the sum of the masses of one hexameric $Cbln1_{FL}$ (134.0 ± 0.2 kDa) and one β-NRX1(+4) (26.13 ± 0.28 kDa) (Fig. S12B).

Together, our ITC (Fig. S12A), MALS (Fig. S12B) and EM (Fig. 1D, 2D and S10) results are dismissive of a 2-to-1 β-NRX1(+4)–$Cbln1_{FL}$ stoichiometry, which was previously suggested (*18, 88*).

Biophysical Analysis of the Cbln1–GluD2 Complex Formation

The $Cbln1_{FL}$–$GluD2_{ATD}$ interaction is independent of β-NRX1 binding (*16, 18*). We measured an apparent K_D ($K_{D,app}$) of ~125 nM for the interaction of β-NRX1(+4)–$Cbln1_{FL}$ and detergent-solubilized $GluD2_{FL}$ using SPR (Fig. S5A). This strong apparent interaction is consistent with a previous report (*18*) but results from avidity effects stemming from the oligomeric nature of $Cbln1_{FL}$ (hexamer) and $GluD2_{FL}$ (dimer of dimers).

Therefore, we dissected the Cbln1–GluD2 complex into the minimal units needed for interaction, and determined their interaction strength.

We first determined, in a domain deletion experiment, that the Cbln C1q domain is the minimal unit needed for interaction with the GluD2 ATD (Fig. S5C).

We then engineered a monomeric $GluD2_{ATD}$ by mutating Phe76 (equivalent to Phe71 in GluA2 (*28*)) to Asp (Fig. S1 and S6A). Phe76Asp (F76D) disrupts Van der Waals (VdW)

contacts with Ala^{111}*, Leu^{108}* and Val^{79}* (* denotes contributions from the second GluD2$_{ATD}$ monomer) through electrostatic repulsion. Mass determination confirmed that GluD2$_{ATD}$-F76D is monomeric, with a mass half that of GluD2$_{ATD}$ (46.4 ± 0.6 kDa vs. 92.7 ± 0.6 kDa, respectively) (Fig. S6B). Likewise, GluD1$_{ATD}$-F73D (GluD1 Phe73 is equivalent to GluD2 Phe76) has a mass half that of GluD1$_{ATD}$ (46.2 ± 0.8 kDa vs. 92.1 ± 0.3 kDa, respectively) (Fig. S6B).

We confirmed the lack of GluD2$_{ATD}$-F76D dimerization via analytical ultracentrifugation (AUC). Wild-type GluD2$_{ATD}$ has a dimer dissociation constant ($K_{D,dimer}$) of 29.7 ± 3.5 nM and no species larger than the dimer (4.00 S) were detected. GluD2$_{ATD}$-F76D sedimented at 2.80 S and remained exclusively monomeric at the highest concentration tested of 100 μM (Fig. S6C).

We injected monomeric GluD2$_{ATD}$-F76D over surface-immobilized Cbln1$_{C1q}$ and observed a generally very weak interaction with no saturation of binding in a concentration range up to 40 μM (Fig. S6D). The same results were obtained when a GluD1$_{ATD}$-F73D construct was tested in a control experiment (Fig. S6E). Multi-cycle kinetics (MCK) analysis of the top-hat function shaped sensorgrams confirmed very fast dissociation kinetics ($k_{off} \geq 0.5$ sec^{-1}; $t_{1/2} <$ 1.5 sec) that prevented accurate K_D determination (Fig. S6D and S6E).

Engineering of a Cbln1–GluD2 Complex Chimera

The weak affinity of the Cbln1$_{C1q}$–GluD2$_{ATD}$ interaction (Fig. S5C) hampered our co-crystallization attempts. Nevertheless, analysis of the individual free structures allowed us to design a construct that linked a Cbln1$_{C1q}$ trimer with GluD2$_{ATD}$ into one continuous polypeptide chain as follows:

(i) N- and C-termini within the Cbln1$_{C1q}$ trimer are spatially close (~17 Å, Fig. S4C). This geometry allowed us to interconnect the three individual C1q monomers (Ser^{59}-Leu^{193}) by using short six-amino acid linkers (GSELGS and GSASGS in single-letter amino acid code, respectively), to form the continuous polypeptide Cbln1$_{C1q\text{-}fused}$ (Fig. 1A and S7). A similar approach has been used for making a single-chain trimer of the structurally related C1q-like protein adiponectin (*89*). Mass determination and inspection of the elution profile via MALS confirmed that, identically to Cbln1$_{C1q}$ (59.8 ± 1.0 kDa) (Fig. S4B), the Cbln1$_{C1q\text{-}fused}$ chimera is trimeric (56.4 ± 2.9 kDa) (Fig. S8B).

(ii) We then developed a strategy to further fuse Cbln1$_{C1q\text{-}fused}$ to GluD2$_{ATD}$. A GluD2$_{ATD}$ dimer is ~85 Å (wide) by 75 Å (high) by 50 Å (deep), while a Cbln1$_{C1q}$ trimer can roughly fit in a

~50 Å diameter sphere. We linked $Cbln1_{C1q\text{-}fused}$ to $GluD2_{ATD}$ by a 30-residue flexible Gly-Gly-Ser ($(G_2S)_{10}$) spacer, which may reach ~110 Å in length in a fully extended conformation and would allow quasi-unrestricted conformational sampling of the $GluD2_{ATD}$ by $Cbln1_{C1q\text{-}fused}$ during the crystallization process. We screened both possible orientations ($Cbln1_{C1q\text{-}fused}$ N- or C-terminal of $GluD2_{ATD}$) and settled on a well-expressing construct where $Cbln1_{C1q\text{-}fused}$ was fused to the N-terminus of $GluD2_{ATD}$ to yield the $Cbln1_{C1q\text{-}fused}$–$GluD2_{ATD}$ chimera (Fig. 1A and S7). The subunit stoichiometry in the chimera is one $Cbln1_{C1q}$ trimer for one $GluD2_{ATD}$ monomer, *i.e.* the minimal interaction unit derived via SPR (Fig. S5C and S6D).

$Cbln1_{C1q\text{-}fused}$–$GluD2_{ATD}$ was purified by IMAC, followed by SEC in 10 mM HEPES, pH 7.0, 150 mM sodium chloride and 3 mM calcium chloride.

The dimeric $GluD2_{ATD}$ drives dimer formation of two $Cbln1_{C1q\text{-}fused}$–$GluD2_{ATD}$ chimeras. The $Cbln1_{C1q\text{-}fused}$–$GluD2_{ATD}$ mass (187.0 ± 1.6 kDa) agrees with the combined masses of one $GluD2_{ATD}$ dimer (92.7 ± 0.6 kDa) and two individual $Cbln1_{C1q\text{-}fused}$ molecules (56.4 ± 2.9 kDa) (Fig. S8B). We further confirmed the $Cbln1_{C1q\text{-}fused}$–$GluD2_{ATD}$ composition by single-particle negative-stain EM; two Cbln1 C1q domains are clearly visible proximal to a central $GluD2_{ATD}$ dimer in individual particles (Fig. S8C). As expected, their conformational variability, due to the presence of the $(G_2S)_{10}$ linker, precluded meaningful particle classification.

We note that in the crystal structure, the distance between the $Cbln1_{C1q}$ C-terminus and $GluD2_{ATD}$ N-terminus is ~45 Å, showing that our $(G_2S)_{10}$ spacer was of sufficient length. Importantly, the linkers interconnecting the C1q monomers, as well as the long $(G_2S)_{10}$ linker, were not visible in the electron density, suggesting that they are disordered and do not interfere with formation of the native interface or impose a certain orientation.

Our $Cbln1_{C1q\text{-}fused}$–$GluD2_{ATD}$ structure shows how Cbln1 engages the membrane-distal GluD2 flap loop, providing a structural explanation for previous binding and mutagenesis experiments (*90*).

Structural Details of the GluD2 Dimer-of-dimers ATD Interface

The GluD2 AB–CD ATD arrangement is, as in $GluA2_{CRYST}$, stabilized by two-fold symmetrical contacts between the D–B monomers (666 $Å^2$ BSA, Fig. 2A and S11A). Glu^{245} and Glu^{248} on α-helix 7 form putative salt bridges with Arg^{275}* on α-helix 8*, the Val^{252} main chain carbonyl oxygen forms a putative hydrogen bond with Tyr^{405}*, and Phe^{254} and Phe^{254}* are engaged in a π-

π sandwich stacking interaction. Furthermore, a strong Fo-Fc peak was observed near the C-terminal tip of α-helices 7 and 8. We modeled this peak as a fully occupied calcium atom based on coordination geometry (3 mM $CaCl_2$ was present in all buffers and no other divalent ions were present in the crystallization condition). The putative hexadentate coordination shell is formed by the carbonyl oxygen atoms of Val^{274}*, Arg^{275}* and Ser^{277}* on α-helix 8*, the carbonyl oxygen atoms of Val^{247} and Glu^{248} on α-helix 7, and the amide oxygen of Asn^{250}. We observed that omission of $CaCl_2$ from the SPR running buffer severely reduced the binding responses (Fig. S11B; detergent-solubilized $GluD2^{\Delta ATD}$ was immobilized in the reference channel). We propose that this is likely due to a lowered active population of GluD2 on the chip surface, since the $Cbln1_{C1q}$–$GluD2_{ATD}$ interaction itself is not dependent on calcium. Interestingly, calcium ions also structurally stabilize the dimerization interface of the GluD2 LBD (*91*).

Design of the $GluD2^{ATD\text{-}LBD\_GLYCAN\_WEDGE}$ Receptor Mutant

Recent EM structures of full-length AMPA receptors ($GluA_{EM}$; (*27*)) have shown that the ATD and LBD layers are more vertically separated from each other compared to the $GluA2_{CRYST}$ crystal structure (*5*) when native, longer linkers instead of engineered, truncated linkers are included. Additionally, it is well known that in NMDA receptors, the ATD provides allosteric control over the LBD (*85*-*87*). Indeed, the crystal structure of the GluN1–GluN2B heteromeric NMDA receptor (*2, 3*) shows a close structural association of ATD and LBD.

Given that (i) Cbln1 binds the GluD2 ATD (Fig. 1B), and (ii) presence of Cbln1 is required for D-Ser mediated signaling via the LBD (Fig. S20), we hypothesized that such ATD-LBD "information transfer" (or "mechanical coupling") is also present in GluD2. We thus constructed the glycan wedge mutant inspired by the observation that longer ATD-LBD linkers can vertically separate the ATD and LBD layers. The ATD-LBD layer separation cannot interfere with the $Cbln1_{C1q}$–$GluD2_{ATD}$ interface, which is located on the opposite side of the ATD. As shown in Fig. 4B, increasing ATD-LBD linker length indeed abolished induction of LTD.

Structure-guided GluD2 Mutants Impact on Synapse Formation and Synaptic Plasticity

Although the total number of PF synapses is reduced in *Grid2*-null mice expressing several mutant GluD2 constructs, the actual number of synapses activated by PF stimulation is considered comparable since the initial PF-EPSC amplitudes were adjusted to be similar. Thus,

the failure to induce D-Ser dependent LTD is unlikely to be attributable to reduced number of PF-PC synapses. We also previously reported that LTD was impaired despite the normal number of PF-PC synapses in *Grid2*-null PCs expressing GluD2 lacking the C-terminal 7 amino acids ($GluD2^{\Delta CT7}$; (*35*)). Indeed, application of exogenous D-Ser failed to induce AMPA receptor endocytosis in *Grid2*-null PCs expressing $GluD2^{\Delta CT7}$ (*8*).

Basic synaptic parameters, such as rise time and desensitization kinetics, are unchanged in *Grid2*-null and *Cbln1*-null Purkinje cells (*21, 35*). The only affected parameter at parallel fiber synapses is the paired-pulse facilitation, which does not mediate postsynaptic AMPA receptor endocytosis and LTD.

Implications for Brain-wide Modulation of GluD Signaling by Cbln

GluD2 expression is confined to PF-PC synapses, while GluD1 (*92, 93*) and Cbln1-4 (*81*) are expressed in various brain regions, in broad and overlapping spatio-temporal patterns. The Cbln–GluD interaction thus likely plays important roles in multiple neuronal circuits. The subtle divergences in Cbln amino acid composition appear sufficient to direct subtype specificity for NRX and GluD variants (*94, 95*). Furthermore, heteromeric Cbln assemblies have also been reported and may further fine-tune interaction specificities (*96*).

Evidence for Other Trans-synaptic Complexes of iGluRs Reveal a Broader Principle

Neuronal C1q-like (C1ql) proteins share a similar domain organization with Cbln1 and therefore the potential to establish molecular bridges with post-synaptic receptors (*97*). Indeed, extracellular coupling between C1ql isoforms 2 and 3 (C1ql2/3) and the ATD of postsynaptic kainate receptors (KARs) GluK2 and GluK4 has been recently confirmed (*20*). Interestingly, C1ql2 and C1ql3 also bind to a presynaptic neurexin-3 (NRX3) isoform that contains a specific sequence encoded by exon25b in splice site 5 (*20*). The discovery of the NRX3–C1ql2/3–GluK2/4 triad illustrates that the β-NRX–Cbln–GluD complex does not represent an isolated case, but rather a more broadly applicable principle.

Supplementary Figures

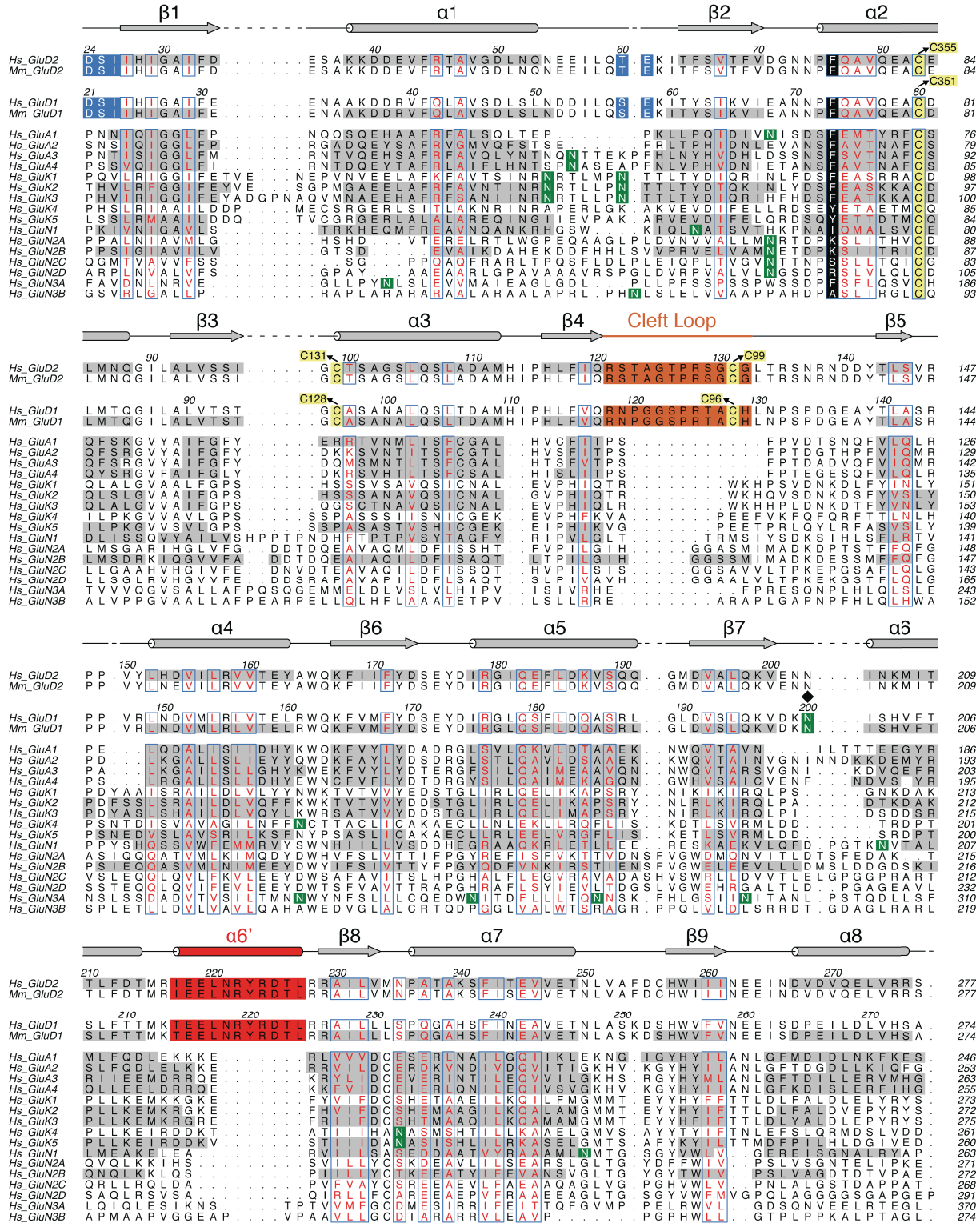

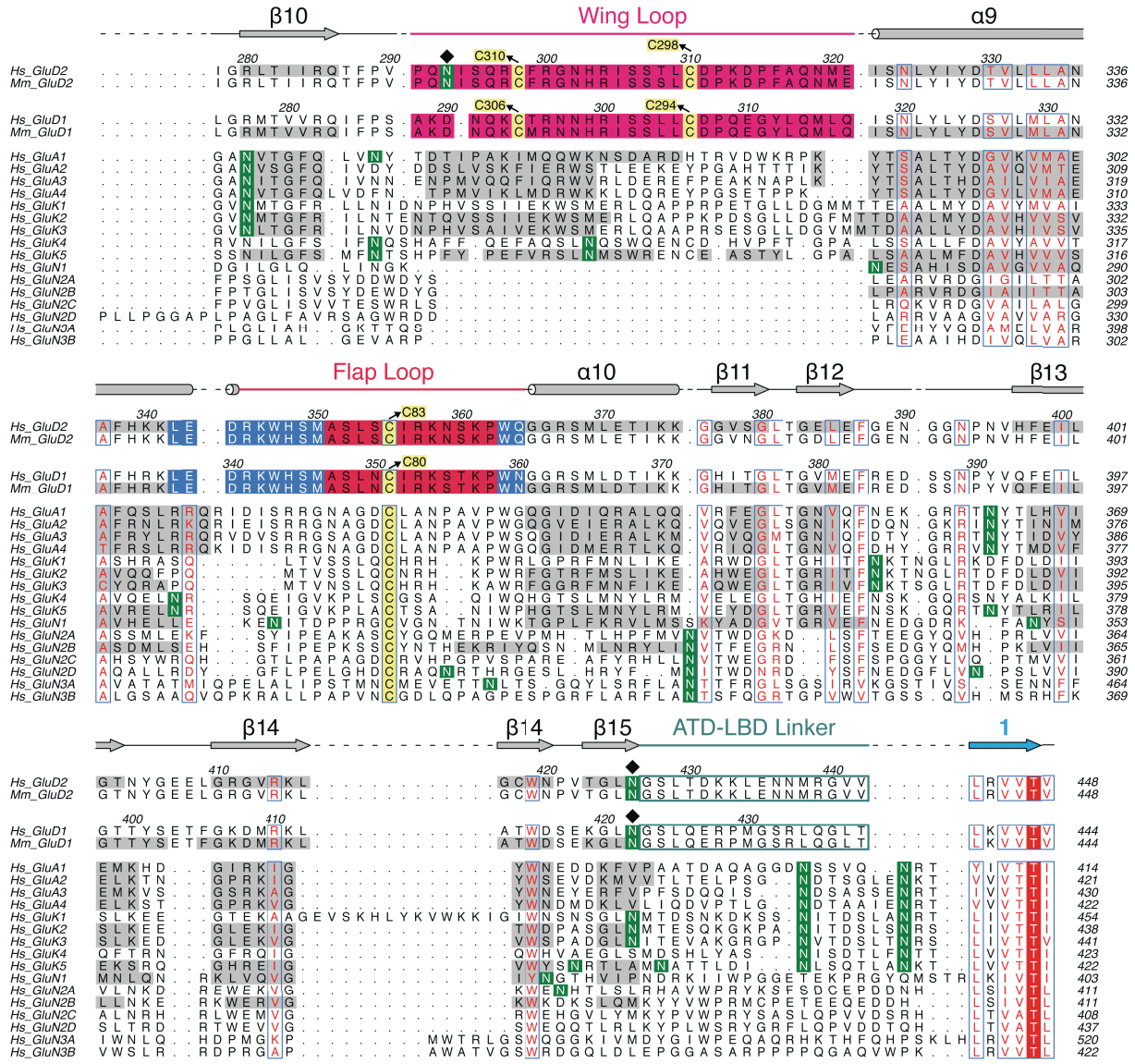

Fig. S1. Structure-based Sequence Alignment of GluD1-2, GluA1-4, GluK1-5 and GluN1-3 Amino-terminal Domains.

Amino acid sequences are taken from the Uniprot database (entry code); *Hs*_GluD2 (O43424), *Mm*_GluD2 (Q61625), *Hs*_GluD1 (Q9ULK0), *Mm*_GluD1 (Q61627), *Hs*_GluA1 (P42261), *Hs*_GluA2 (P42262), *Hs*_GluA3 (P42263), *Hs*_GluA4 (P48058), *Hs*_GluK1 (P39086), *Hs*_GluK2 (Q13002), *Hs*_GluK3 (Q13003), *Hs*_GluK4 (Q16099), *Hs*_GluK5 (Q16478), *Hs*_GluN1 (Q05586), *Hs*_GluN2A (Q12879), *Hs*_GluN2B (Q13224), *Hs*_GluN2C (Q14957), *Hs*_GluN2D (O15399), *Hs*_GluN3A (Q8TCU5), and *Hs*_GluN3B (O60391). *Hs*; *Homo sapiens*, *Mm*; *Mus musculus*. Secondary structure elements for GluD2 are annotated above the alignment

and are shaded in grey for iGluR members for which an ATD crystal structure is available. GluD structural elements are highlighted; cleft loop (orange), α-helix 6' (red), wing loop (pink), flap loop (magenta), ATD-LBD linker (green), and Cbln1–GluD2 complex interface residues (blue). GluD cysteine residues participating in disulfide bonds are shown in yellow boxes. N-linked glycosylation sites for all iGluR members are shown in dark green boxes (black diamonds highlight N-linked GluD glycosylation sites). The first β-strand of the LBD is colored light blue. Phe76 (F76; GluD2 numbering) and structurally equivalent residues are boxed in black. GluD2 α-helix 8 is denoted as η1-η2 in GluA; GluA α-helix 8 occupies the place of the GluD2 wing loop.

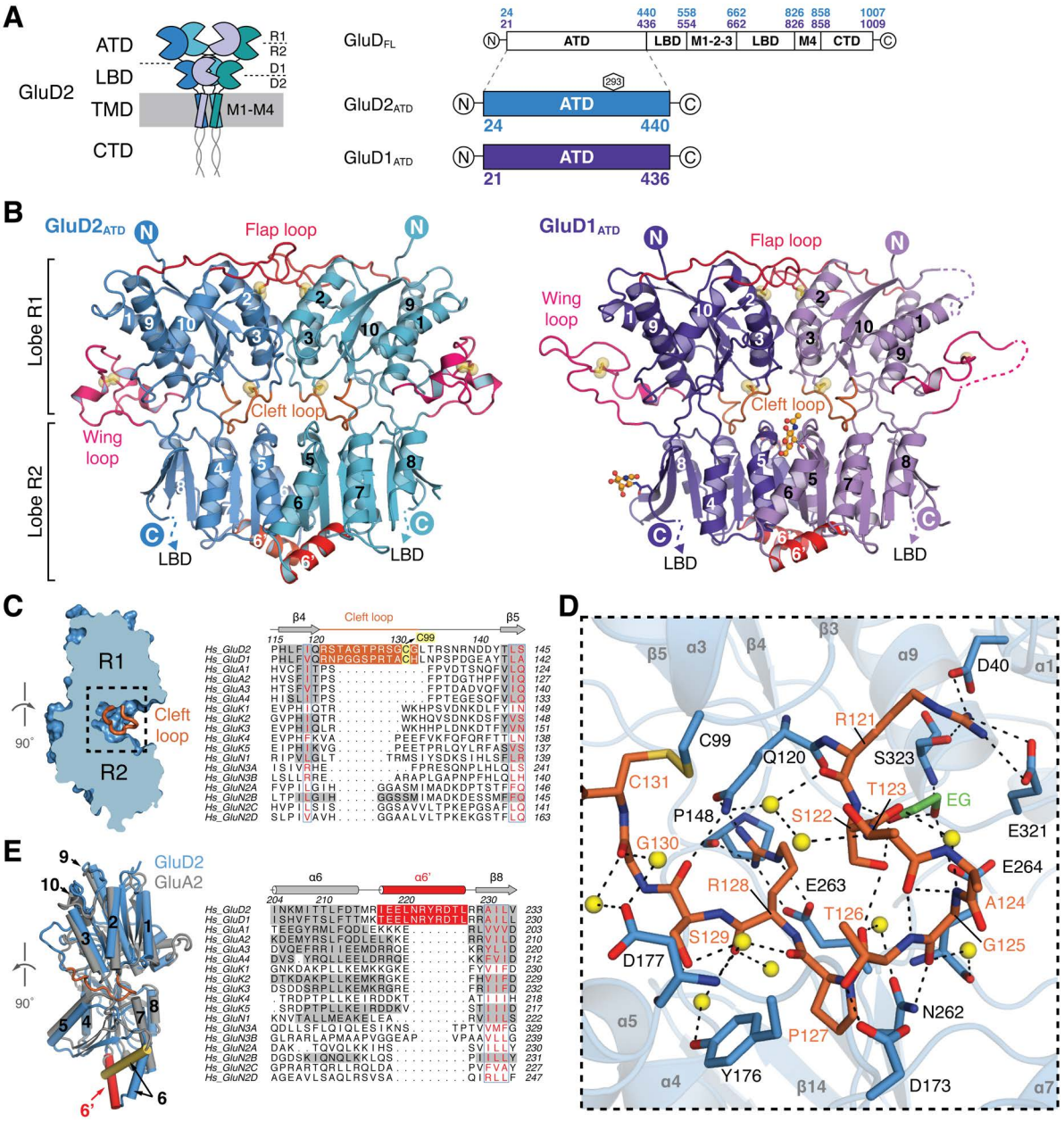

Fig. S2. Crystal Structures of the GluD2 and GluD1 Amino-terminal Domains.

(A) Schematic representation of the GluD2 domain organization and constructs used for structure determination. ATD: amino-terminal domain. LBD: ligand-binding domain. TMD: transmembrane domain. CTD: carboxy-terminal domain. Domain boundaries are annotated. **(B)** Crystal structures of the GluD2$_{ATD}$ (left) and GluD1$_{ATD}$ (right) dimers. α-helix 6' and the flap, wing and cleft loops are highlighted. Disulfide bridges are shown as yellow spheres. N-acetyl glucosamine (NAG) moieties visible in the electron density maps are shown in ball and stick representation. **(C)** Cutout view through the GluD2$_{ATD}$ monomer, 90° rotated (relative to (A));

the cleft loop is highlighted in orange. **(D)** Detailed interactions of the cleft loop (orange) with residues of the R1 and R2 lobes (boxed section in (C)). Water molecules are shown as yellow spheres. Hydrogen bonds and hydrophilic interactions are indicated with black dashed lines. EG: ethylene glycol. **(E)** View of the $GluD2_{ATD}$ monomer, 90° rotated (relative to (A)), superposed on the GluA2 ATD (PDB ID 2WJW (*28*)). GluD2 α-helix 6' is colored red and GluA2 α-helix 6 is colored yellow.

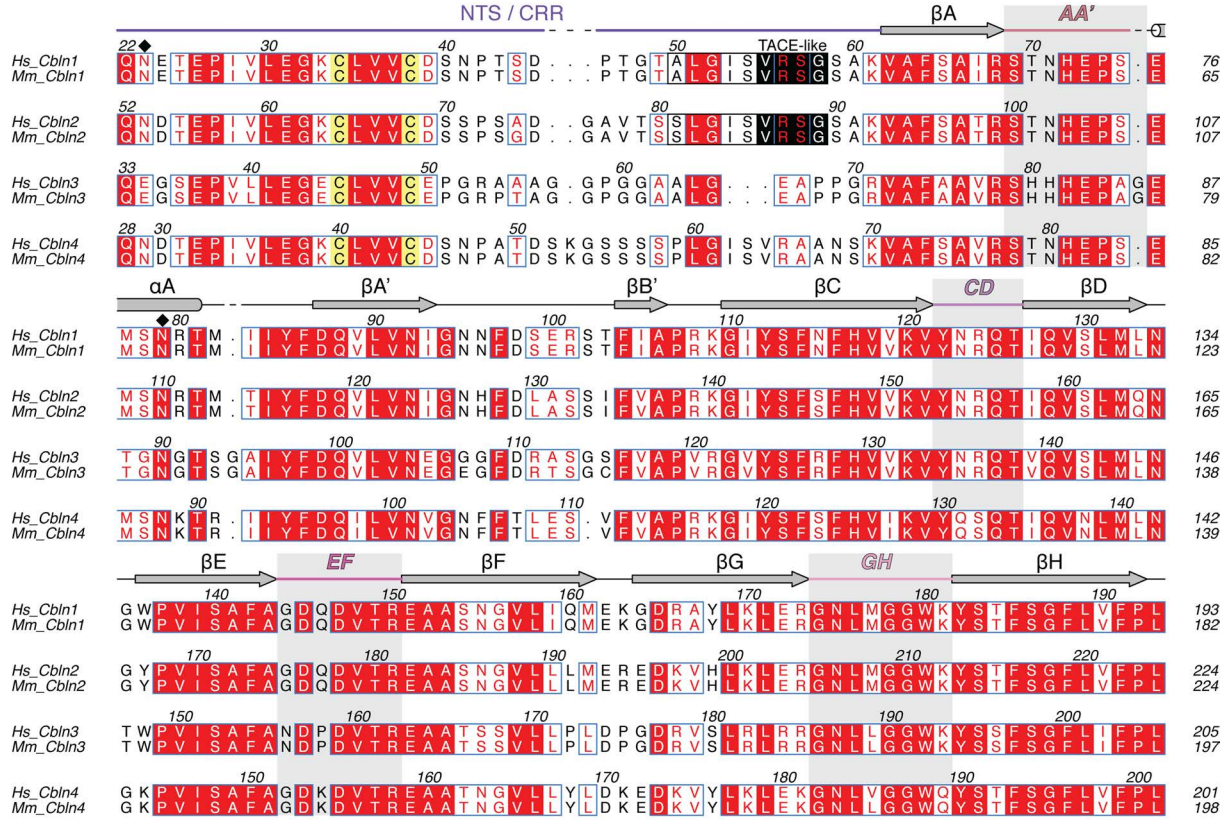

Fig. S3. Sequence Alignment of Human and Mouse Cerebellin Homologs.

Sequence alignment of human (*Hs*; *Homo sapiens*) and mouse (*Mm*; *Mus musculus*) Cbln homologs. Amino acid sequences are taken from the Uniprot database (entry code); *Hs*_Cbln1 (P23435), *Mm*_Cbln1 (Q80W16), *Hs*_Cbln2 (Q8IUK8), *Mm*_Cbln2 (Q8BGU2), *Hs*_Cbln3 (Q6UW01), *Mm*_Cbln3 (Q9JHG0), *Hs*_Cbln4 (Q9NTU7), and *Mm*_Cbln4 (Q8BME9). Secondary structure elements for Cbln1 are annotated above the alignment. Cbln1 loops *AA'*, *CD*, *EF*, *GH* are highlighted in shades of magenta and boxed in grey. The N-terminal segment (NTS) / cysteine-rich region (CRR) is highlighted in purple. Cysteine residues in the NTS / CRR are shown in yellow. The putative Cbln1 and Cbln2 tumor necrosis factor alpha-converting enzyme-like (TACE-like) cleavage sites are boxed in black. Black diamonds indicate Cbln1 N-linked glycosylation sites.

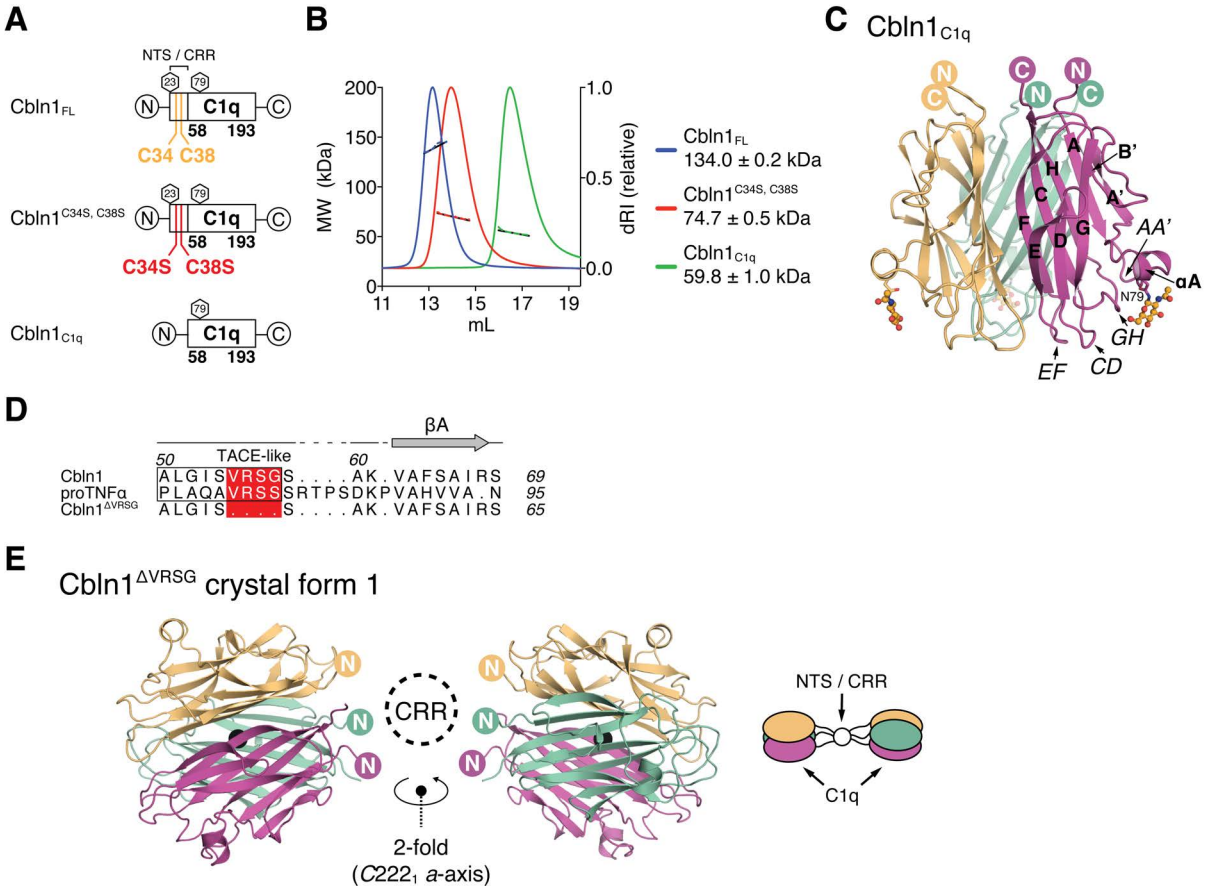

Fig. S4. Crystal Structure of Cbln1.

(A) Schematic representation of Cbln1 constructs. NTS; N-terminal segment. CRR; cysteine-rich region. **(B)** Molecular mass determination of $Cbln1_{FL}$ (blue), $Cbln1^{C34S,\ C38S}$ (red), and $Cbln1_{C1q}$ (green) by MALS. **(C)** Crystal structure of the globular Cbln1 C1q trimer. β-strands and loops are annotated. The N-acetyl glucosamine (NAG) moiety bound to Asn^{79} (N79) is shown in ball-and-stick representation. **(D)** Sequence alignment of TACE-like cleavage sites in Cbln1 and pro-TNFα. **(E)** Crystal structure of the putative TACE-site mutant $Cbln1^{\Delta VRSG}$. The head-to-head dimer-of-trimers structure of Cbln1 is generated through symmetry operation around a crystallographic twofold axis.

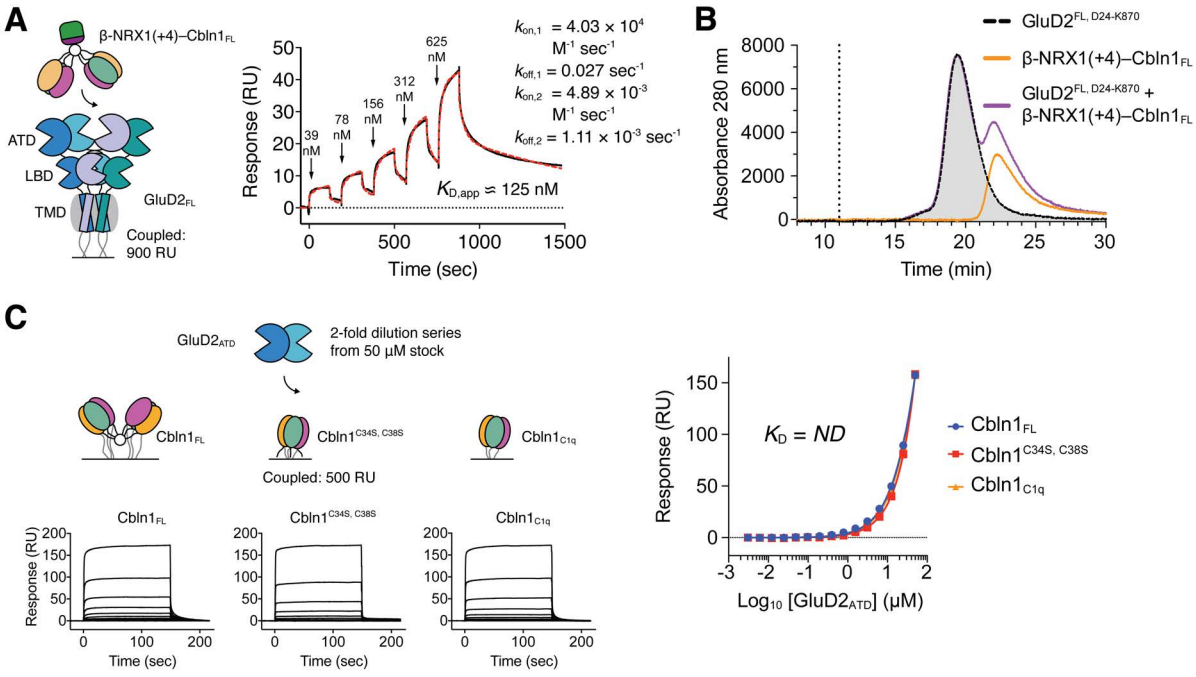

Fig. S5. The Cbln1 C1q Domain Determines Binding to GluD2.

(A) Single-cycle kinetics (SCK) analysis of the interaction between β-NRX1(+4)–Cbln1$_{FL}$ and detergent-solubilized GluD2$_{FL}$. Detergent-solubilized GluD2$^{\Delta ATD,\ D24\text{-}K870}$ was immobilized in the reference channel. **(B)** SEC profile of detergent-solubilized GluD2$^{FL,\ D24\text{-}K870}$, and lack of co-elution with the β-NRX1(+4)–Cbln1$_{FL}$ complex. **(C)** Binding isotherms and sensorgrams for the interactions of GluD2$_{ATD}$ with Cbln1$_{FL}$, Cbln1$^{C34S,\ C38S}$ and Cbln1$_{C1q}$. The Cbln1 C1q trimer is the minimal unit needed for interaction with GluD2.

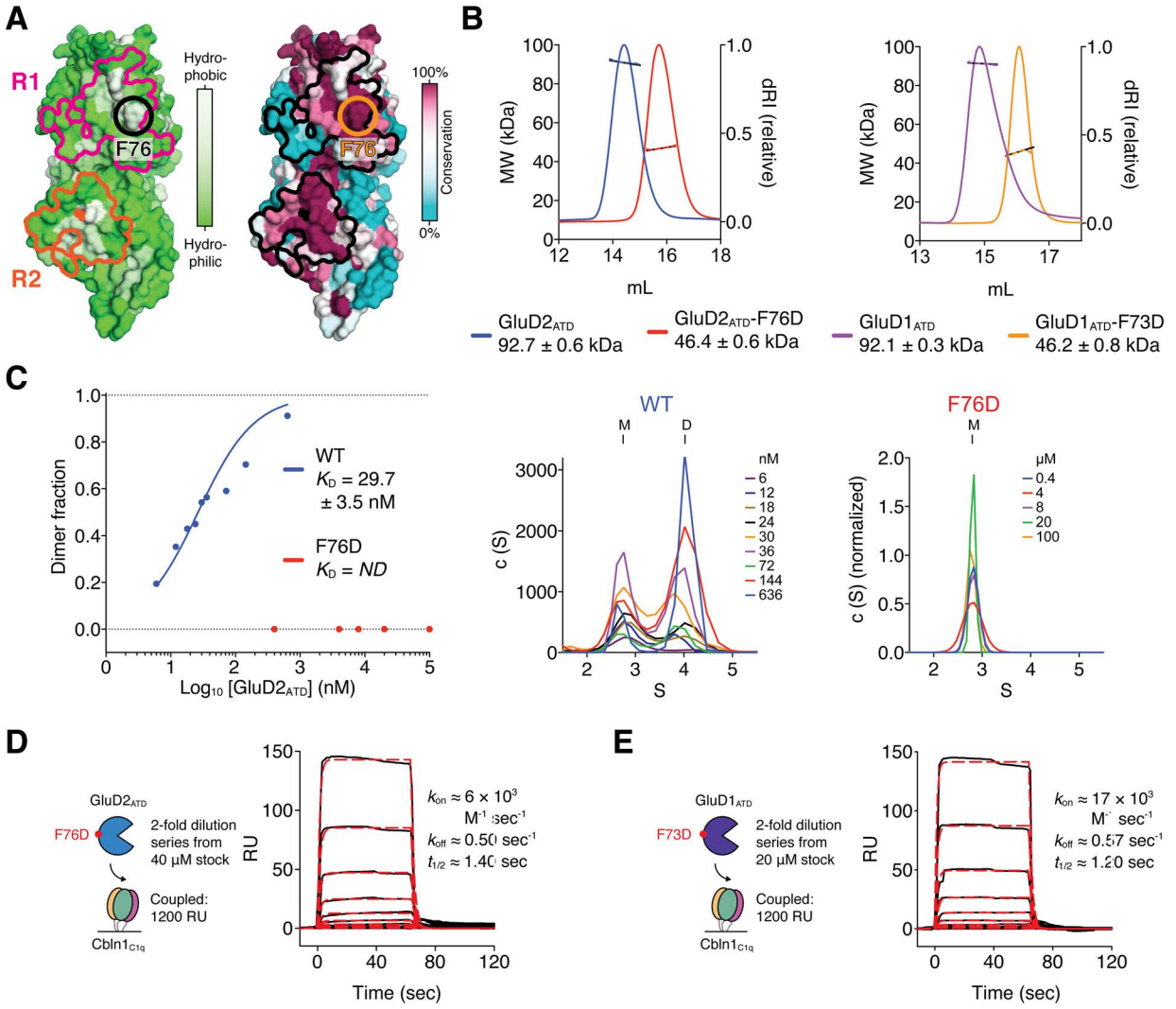

Fig. S6. Engineering of a Monomeric GluD2 and GluD1 Amino-terminal Domain.

(A) View of the GluD2$_{ATD}$ dimer interface. The colored lines outline the total buried dimer interface area formed by the R1 and R2 lobes. The left and right panels depict the GluD2$_{ATD}$ dimer interface color coded by residue hydrophobicity and sequence conservation, respectively. The position of Phe^{76} (F76) is marked with a circle. **(B)** Molecular mass determination of the GluD2$_{ATD}$ dimer (blue), GluD2$_{ATD}$-F76D monomer (red), GluD1$_{ATD}$ dimer (purple) and GluD1$_{ATD}$-F73D monomer (orange) by MALS. **(C)** Determination of the dissociation constant of ATD dimer formation ($K_{D,dimer}$) for GluD2$_{ATD}$ (blue) and GluD2$_{ATD}$-F76D (red) by AUC. The middle and right panels show the sedimentation data for the GluD2$_{ATD}$ and GluD2$_{ATD}$-F76D concentration series, respectively. M; monomer, D; dimer. The GluD2$_{ATD}$ $K_{D,dimer}$ value (29.7 nM) is similar to that of GluK2/5 heterodimers (11 nM) (*98*), and GluA4 homodimers

(10 nM) (*99*). **(D-E)** Multi-cycle kinetics sensorgrams and fits for the interaction of (D) $GluD2_{ATD}$-F76D and (E) $GluD1_{ATD}$-F73D with $Cbln1_{C1q}$. Fast dissociation kinetics ($k_{off} \geq 0.5$ sec^{-1}) prevented accurate K_D determination.

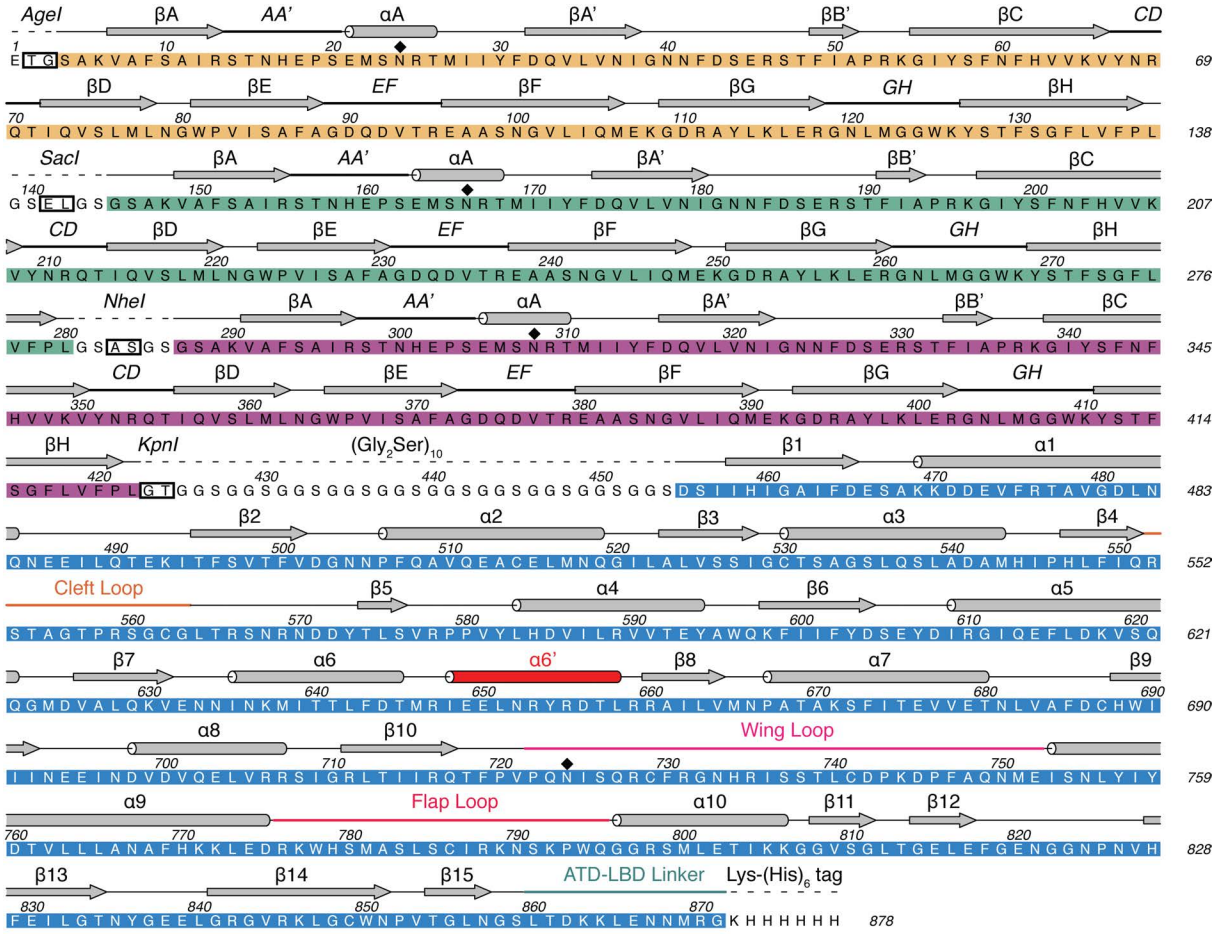

Fig. S7. Detailed Sequence of the Cbln1$_{C1q\text{-}fused}$–GluD2$_{ATD}$ Chimera.

Secondary structure elements for Cbln1$_{C1q}$ and GluD2$_{ATD}$, derived from the Cbln1$_{C1q\text{-}fused}$–GluD2$_{ATD}$ chimera crystal structure, are annotated above the sequence. Numbering corresponds to the full, mature sequence of the expression construct (878 amino acids in total). Consecutive Cbln1$_{C1q}$ sequences of the Cbln1$_{C1q\text{-}fused}$ chimera are colored yellow, green, and magenta. GluD2$_{ATD}$ is colored blue. GluD2 structural elements are highlighted; cleft loop (orange), α-helix 6' (red), wing loop (pink), flap loop (magenta) and ATD-LBD linker (green). Footprints of cloning sites are indicated with a black box and are annotated. Black diamonds indicate N-linked glycosylation sites. The GSELGS, GSASGS and $(G_2S)_{10}$ linkers, and the C-terminal Lys-$(His)_6$ tag are indicated with dashed lines.

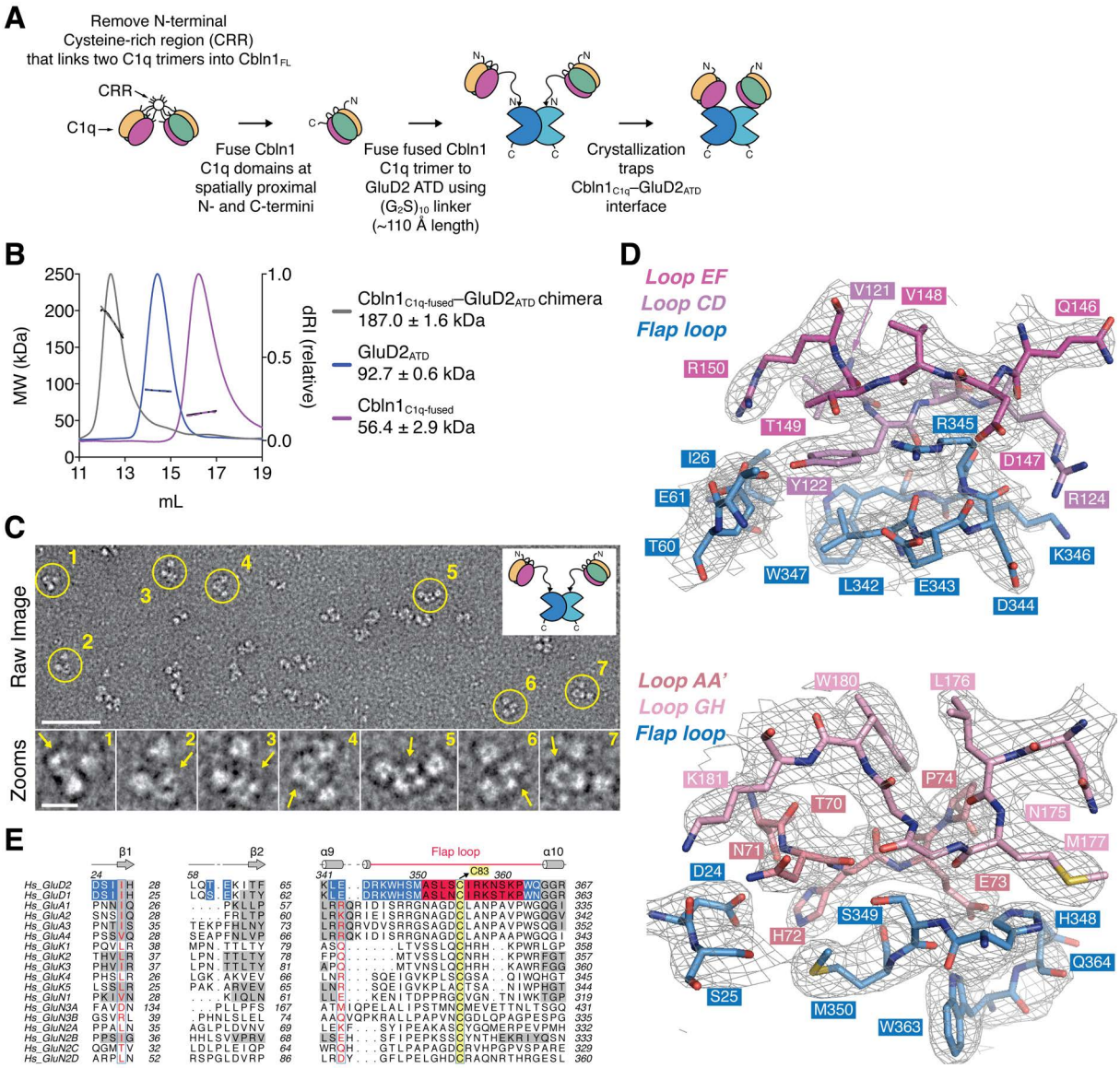

Fig. S8. Analysis of the Cbln1$_{C1q}$–GluD2$_{ATD}$ Complex.

(A) Schematic representation of the construction and structure determination of the Cbln1$_{C1q\text{-}fused}$–GluD2$_{ATD}$ chimera. **(B)** Molecular mass determination of Cbln1$_{C1q\text{-}fused}$ (purple), GluD2$_{ATD}$ (blue) and the Cbln1$_{C1q\text{-}fused}$–GluD2$_{ATD}$ chimera (gray) by MALS. The dimeric GluD2$_{ATD}$ drives dimerization of the Cbln1$_{C1q\text{-}fused}$–GluD2$_{ATD}$ chimera. **(C)** Negative-staining single-particle EM of the Cbln1$_{C1q\text{-}fused}$–GluD2$_{ATD}$ chimera. A representative part of a raw EM micrograph is shown (scale bar; 50 nm) and selected individual particles are highlighted and magnified (lower band; scale bar; 10 nm). Conformational variability prevented meaningful class averaging. The suggested central position of the GluD2$_{ATD}$ dimer in the Cbln1$_{C1q}$–GluD2$_{ATD}$ chimera dimer is indicated with yellow arrows. **(D)** 2*m*Fo-*D*Fc electron density (calculated using PHENIX),

contoured at 1.0 σ, for the final refined model centered at the $Cbln1_{C1q}$–$GluD2_{ATD}$ interaction interface. The top and bottom panels detail the interactions made by Cbln1 loops *EF* and *CD*, and loops *AA'* and *GH*, respectively. **(E)** Sequence alignment of human iGluRs, focusing on the GluD regions involved in Cbln binding. Interface residues are highlighted in blue boxes.

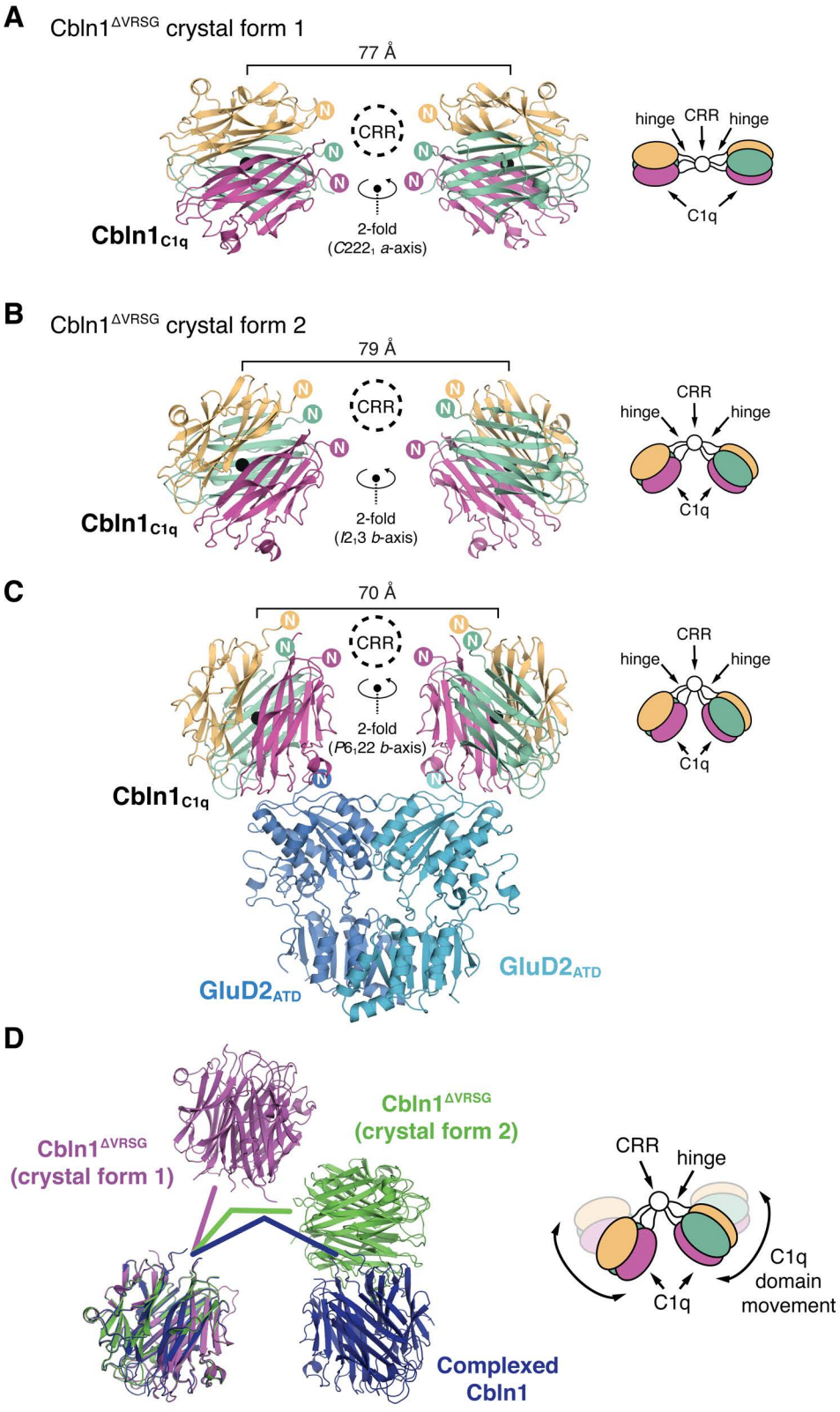

Fig. S9. Structural Comparison of Free and GluD2-bound Cbln1.

(A-B) Crystal structure of free Cbln1$^{\Delta VRSG}$ from two crystal forms. **(C)** Crystal structure of the Cbln1$_{C1q}$–GluD2$_{ATD}$ complex. In each case, the suggested position of the Cbln1 cysteine-rich region (CRR) is indicated by a dashed circle. Black spheres denote the centers of mass of the C1q trimers; in both free and bound Cbln1, the distances between them are comparable (~70-79 Å). The head-to-head orientation of the Cbln1$_{C1q}$ domains in Cbln1$^{\Delta VRSG}$ is more linear than in the Cbln1$_{C1q}$–GluD2$_{ATD}$ complex due to crystal packing and the fact that the Cbln1$_{C1q}$ domains are not conformationally constrained by binding to GluD2$_{ATD}$. The relative orientations of the Cbln1$_{C1q}$ domains in free Cbln1$^{\Delta VRSG}$ structures are selected from the broad range of possible Cbln1 conformations, as observed in the in the single-particle EM classes (Fig. S10). **(D)** Structural alignment of both free Cbln1$^{\Delta VRSG}$ structures with bound Cbln1 using one Cbln1 C1q trimer as reference. The markedly different tilt angles indicate the conformational flexibility of Cbln1.

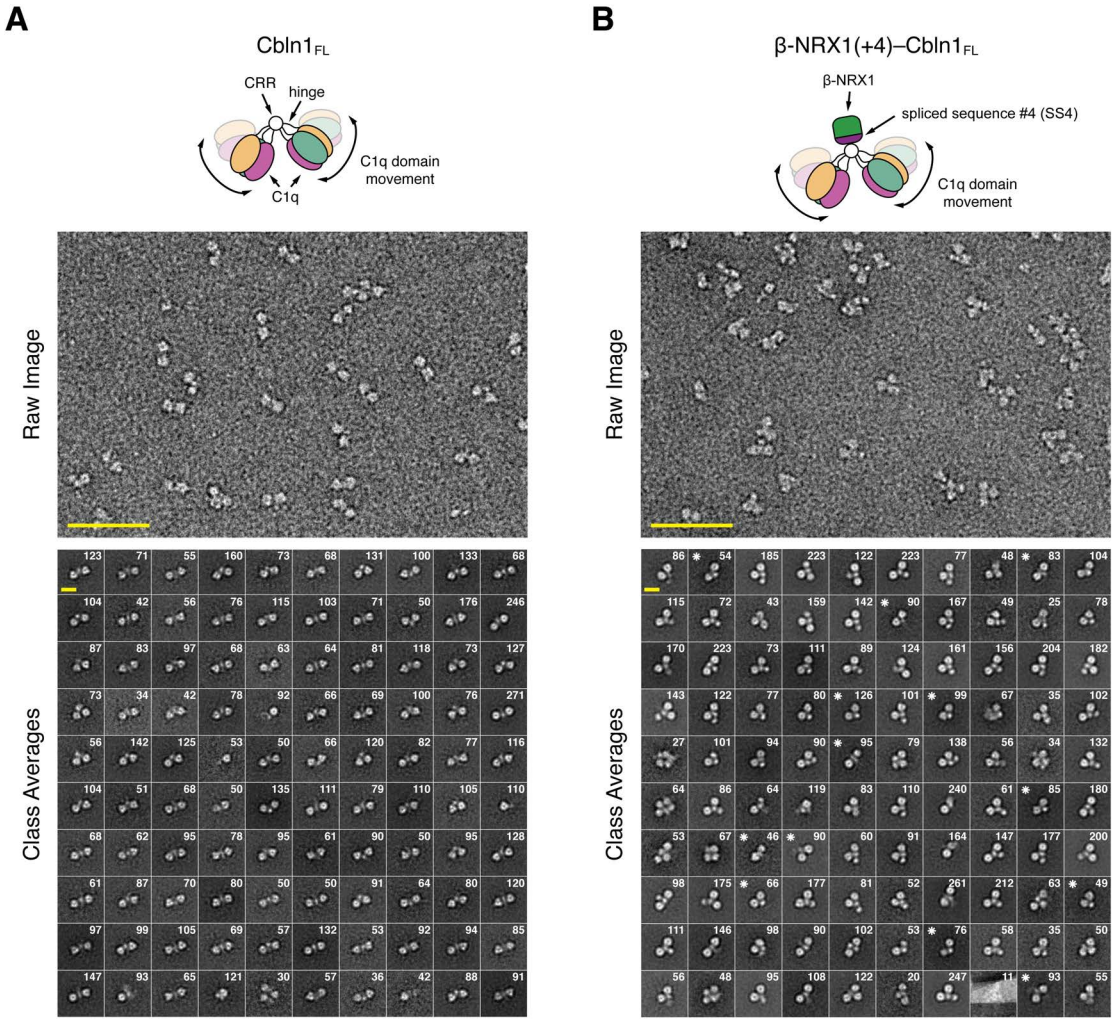

Fig. S10. Electron Microscopic Analysis of Cbln1 and the β-NRX1–Cbln1 Complex.

(A) Negative-stain EM class averages for Cbln1 obtained by classifying 8821 particles into 100 classes (scale bar; 10 nm). A representative part of a raw EM micrograph is shown below the class averages (scale bar; 50 nm). Numbers indicate the number of particles in each class. **(B)** Negative-stain EM class averages for the β-NRX1(+4)–Cbln1 complex obtained by classifying 8475 particles into 100 classes (scale bar; 10 nm). A representative part of a raw EM micrograph is shown below the class averages (scale bar; 50 nm). Numbers indicate the number of particles in each class. Some classes (marked with a white star symbol) likely represent free $Cbln1_{FL}$ particles that dissociated from their complex with β-NRX1(+4) on the EM grid.

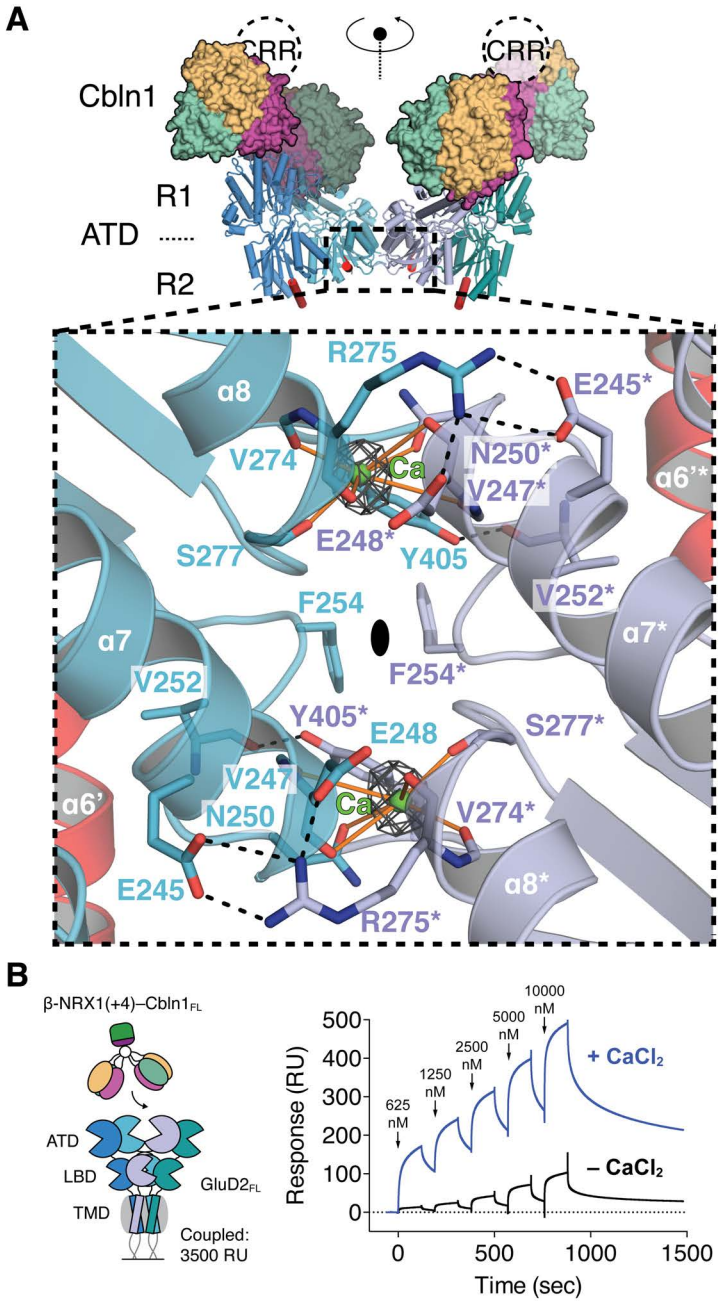

Fig. S11. Structural Details of the GluD2 ATD Dimer-of-dimers Interface.

(A) Detailed view of the $GluD2_{ATD}$ dimer-of-dimers interface. Putative hydrogen bonds and hydrophilic interactions are indicated with black dashed lines. Putative calcium atoms (Ca) are shown as green spheres, and their putative hexadentate coordination is indicated with orange lines. 2*m*Fo-*D*Fc electron density (calculated using PHENIX) for the Ca atoms is shown as a black mesh and contoured at 1.0 σ. **(B)** Single-cycle kinetics (SCK) analysis of the interaction

between β-NRX1(+4)–Cbln1$_{FL}$ and detergent-solubilized GluD2$_{FL}$. Detergent-solubilized GluD2$^{\Delta ATD}$ was immobilized in the reference channel. Omission of $CaCl_2$ in the running buffer reduces the apparent active population of detergent-solubilized GluD2$_{FL}$ on the SPR chip surface.

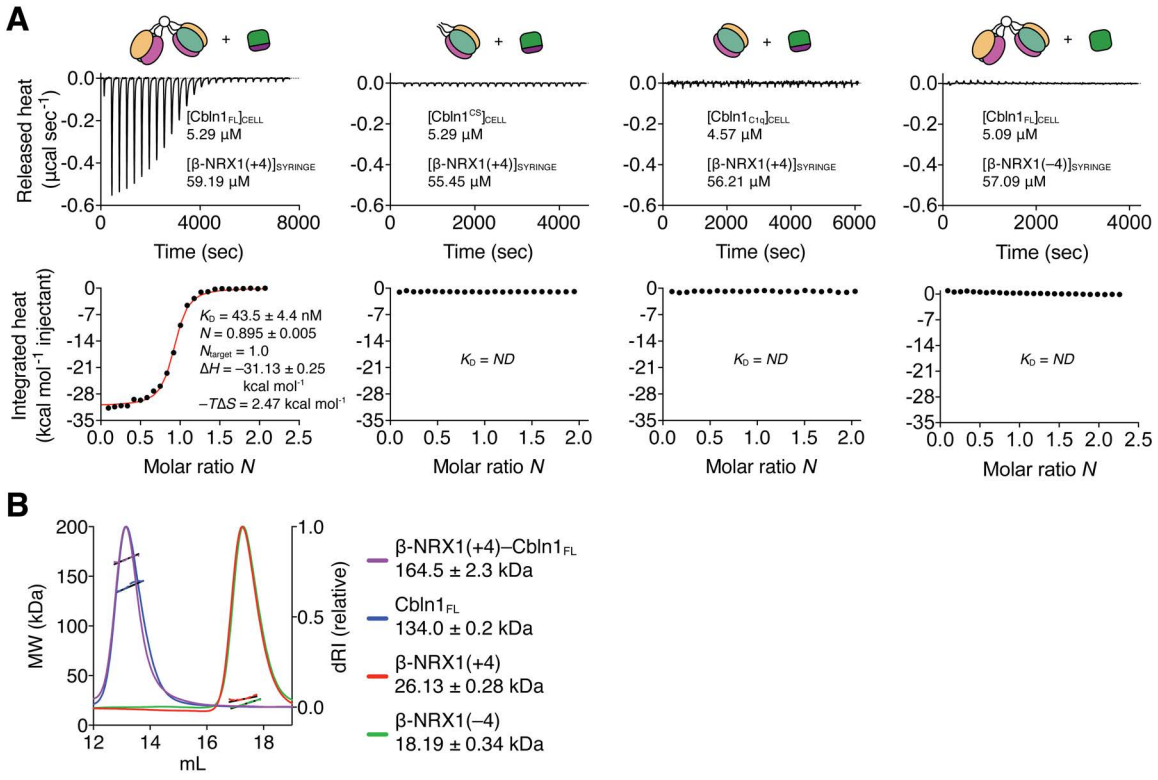

Fig. S12. Stoichiometry of the β-NRX1–Cbln1 Complex.

(A) Thermodynamic profile, affinity and stoichiometry (*N*) of the interaction between Cbln1 and β-NRX1 variants. In each case, the schematic molecular representations correspond to the experimental geometry "cell content" + "syringe content". **(B)** Molecular mass determination of the β-NRX1(+4)–Cbln1$_{FL}$ complex (purple), Cbln1$_{FL}$ (blue), β-NRX1(+4) (red) and β-NRX1(−4) (green) by MALS.

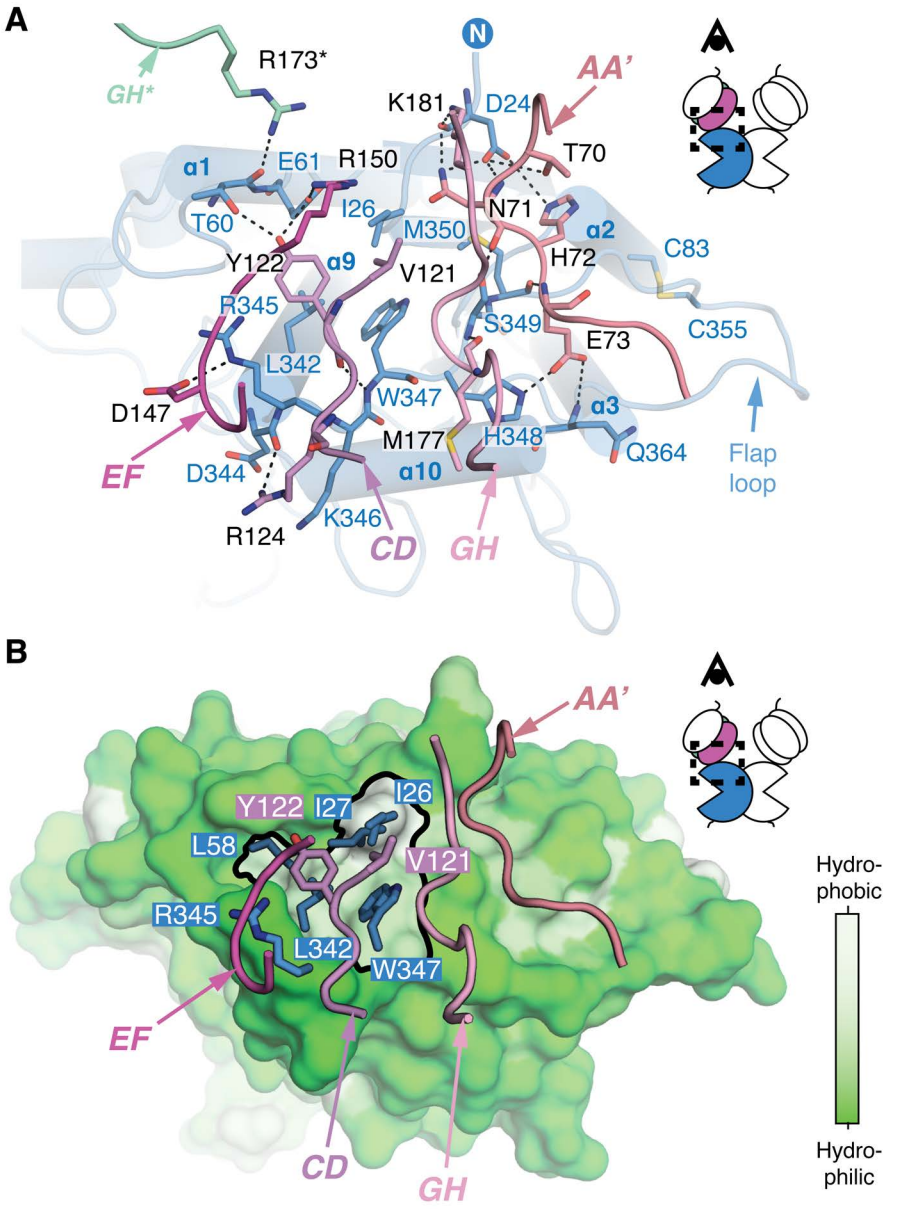

Fig. S13. Details of the Cbln1$_{C1q}$–GluD2$_{ATD}$ Interaction Interface.

(A) Black dashed lines indicate putative hydrogen bonds and hydrophilic interactions. The asterisk (*) denotes limited contributions from a second C1q monomer. **(B)** View of the Cbln1$_{C1q}$–GluD2$_{ATD}$ interface core hydrophobic interactions. Cbln1 Val^{121} and Tyr^{122} are buried in a small hydrophobic pocket formed by GluD2 Ile^{26}, Ile^{27}, Leu^{58}, Leu^{342} and Trp^{347} (outlined in black).

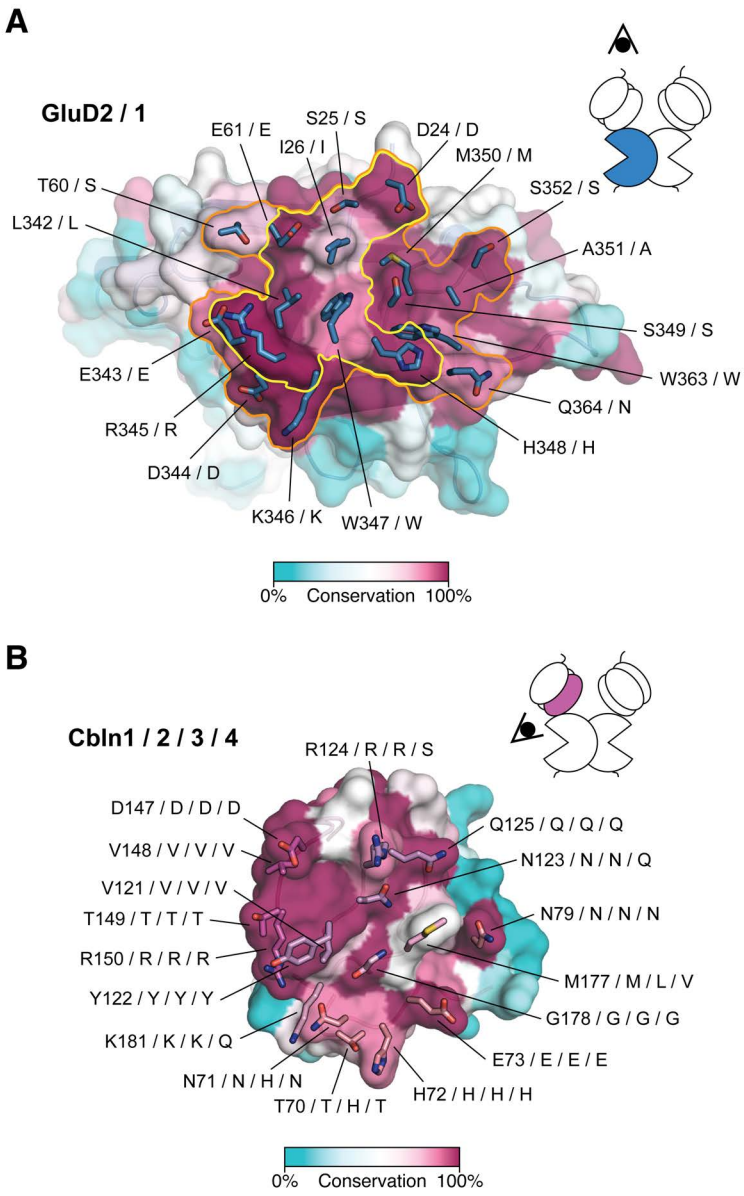

Fig. S14. Sequence Conservation of the GluD$_{ATD}$ and Cbln Interaction Interfaces.

(A) View of the GluD2 interaction interface, color-coded by sequence conservation in vertebrate GluD2 and GluD1 (205 total sequences). Per position, equivalent residues in human GluD2 and -1 are annotated. The total Cbln1–GluD2 interface area is outlined in orange, and the interaction hotspot is outlined in yellow. **(B)** View of the Cbln1 interaction interface, color-coded by sequence conservation in vertebrate Cbln-1, -2, -3 and -4 (330 total sequences). Per position, equivalent residues in human Cbln1, -2, -3, and -4 are annotated.

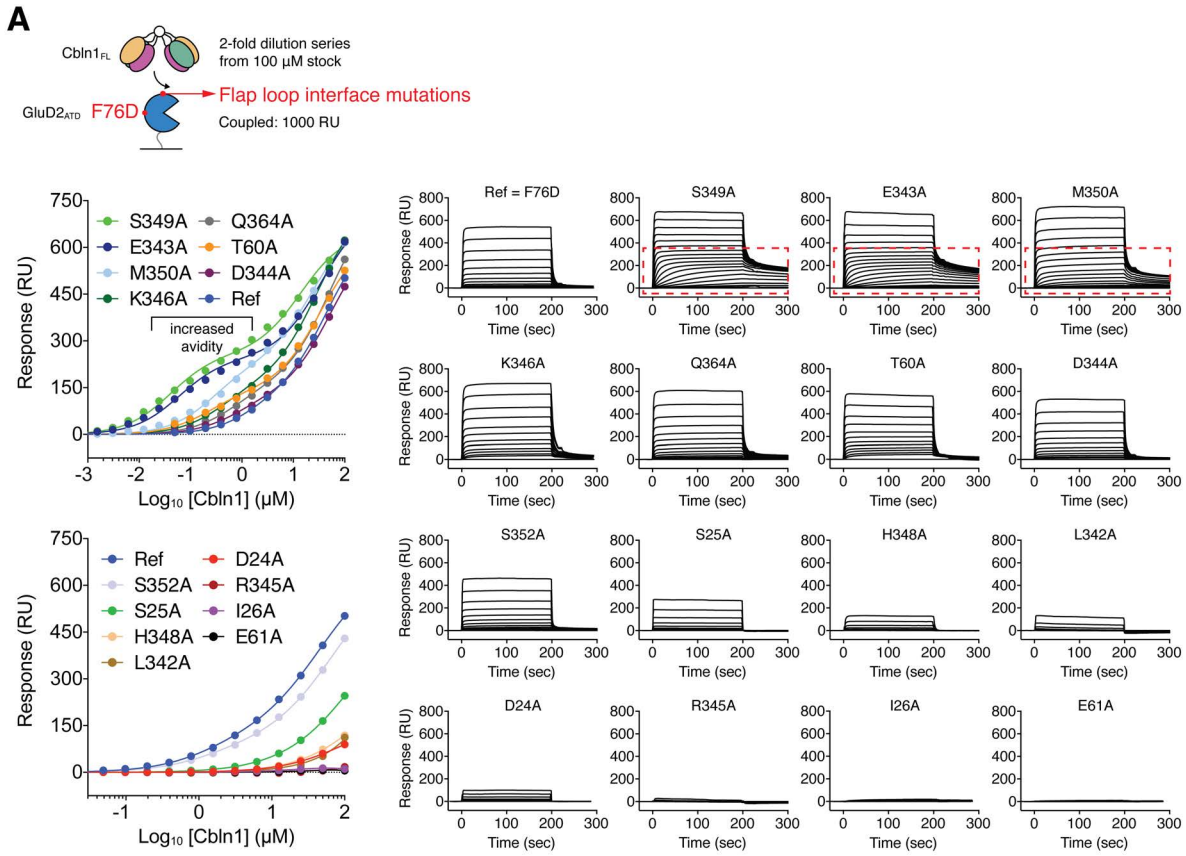

Fig. S15. Mutational Analysis of the GluD2$_{ATD}$ Interface.

(A) Binding isotherms and sensorgrams for the GluD2$_{ATD}$ interface mutants. Point mutations were introduced on the monomeric GluD2$_{ATD}$-F76D backbone ("Ref"; Fig. S6A). Sensorgrams for S349A, E343A and M350A show a nanomolar-range, higher-affinity component to the total binding (red dashed boxes).

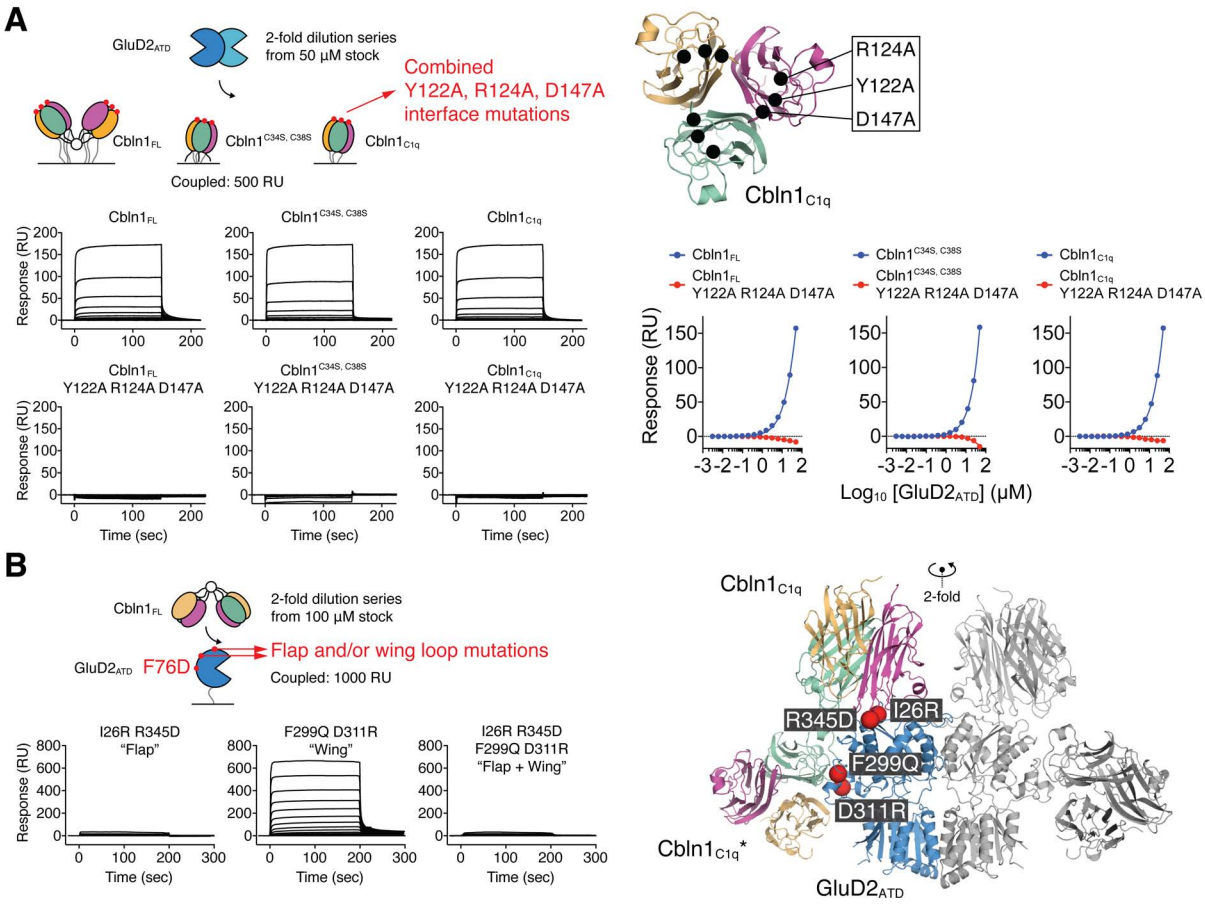

Fig. S16. Mutational Analysis of the Cbln1 Interface and Cbln1–GluD2 Crystal Packing.

(A) Binding isotherms and sensorgrams for the interactions of $GluD2_{ATD}$ with $Cbln1_{FL}$, $Cbln1^{C34S,\ C38S}$, $Cbln1_{C1q}$ and their corresponding Y122A-R124A-D147A interface mutants. Wild-type interactions are repeated here from Fig. S5C for clear comparison. **(B)** Sensorgrams for the $GluD2_{ATD}$ flap (I26R, R345D double mutant), wing (F299Q, D311R double mutant) and combined mutants. The asterisk (*) denotes a symmetry-related C1q domain contacting the $GluD2_{ATD}$ "wing" loop.

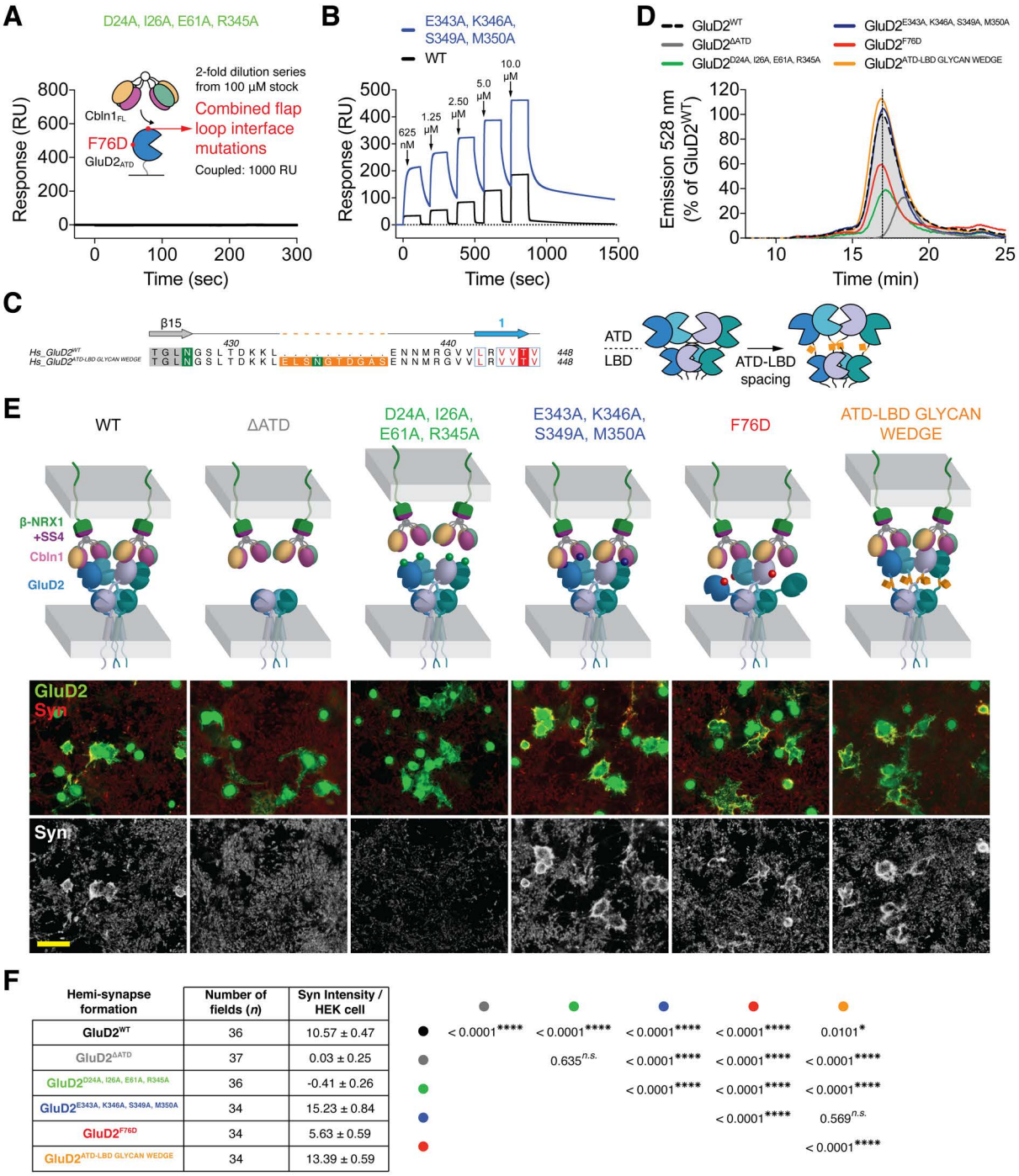

Fig. S17. Structure-guided GluD2 Mutants Impact on Synapse Formation *In Vitro*.

(A) Sensorgrams for the combined D24A, I26A, E61A, R345A $GluD2_{ATD}$ interface mutant. Point mutations were introduced in the $GluD2_{ATD}$-F76D backbone. **(B)** Single-cycle kinetics (SCK) analysis of the interaction between $Cbln1_{FL}$ and (i) $GluD2_{ATD}$ ($GluD2_{ATD}$-F76D; "Ref"; Fig. S15A), or (ii) the combined E343A, K346A, S349A, M350A $GluD2_{ATD}$ interface mutant

(constructed on the $GluD2_{ATD}$-F76D backbone). The combined D24A, I26A, E61A, R345A $GluD2_{ATD}$ interface mutant was immobilized in the reference channel. **(C)** Sequence and schematic representation of the $GluD2^{ATD\text{-}LBD\_GLYCAN\_WEDGE}$ linker mutant. Putative N-linked glycosylation sites are colored green. **(D)** Fluorescence-detection size-exclusion chromatography (FSEC) profile of detergent solubilized $GluD2^{WT}$, $GluD2^{\Delta ATD}$, $GluD2^{D24A,\ I26A,\ E61A,\ R345A}$, $GluD2^{E343A,\ K346A,\ S349A,\ M350A}$, $GluD2^{F76D}$ and $GluD2^{ATD\text{-}LBD\_GLYCAN\_WEDGE}$, all truncated at Lys^{870}. GluD2 receptors were C-terminally tagged with monoVenus (mVenus). **(E)** Hemi-synapse formation assay of cerebellar granule cells (GC) co-cultured with HEK 293T cells expressing wild-type GluD2 and structure-guided GluD2 mutants. Representative confocal images of HEK 293T cells immunostained for GluD2 (green) and GC axon terminals immunostained for synaptophysin (Syn; red and white) are shown. Scale bar: 50 μm. **(F)** Summary of HEK 293T cell and cerebellar granule cell (GC) hemi-synapse formation assay values and statistics. *p* values were obtained using a Kruskal-Wallis test followed by a Steel-Dwass test. ****; $p < 0.0001$, *; $p < 0.05$, *n.s.*; not significant.

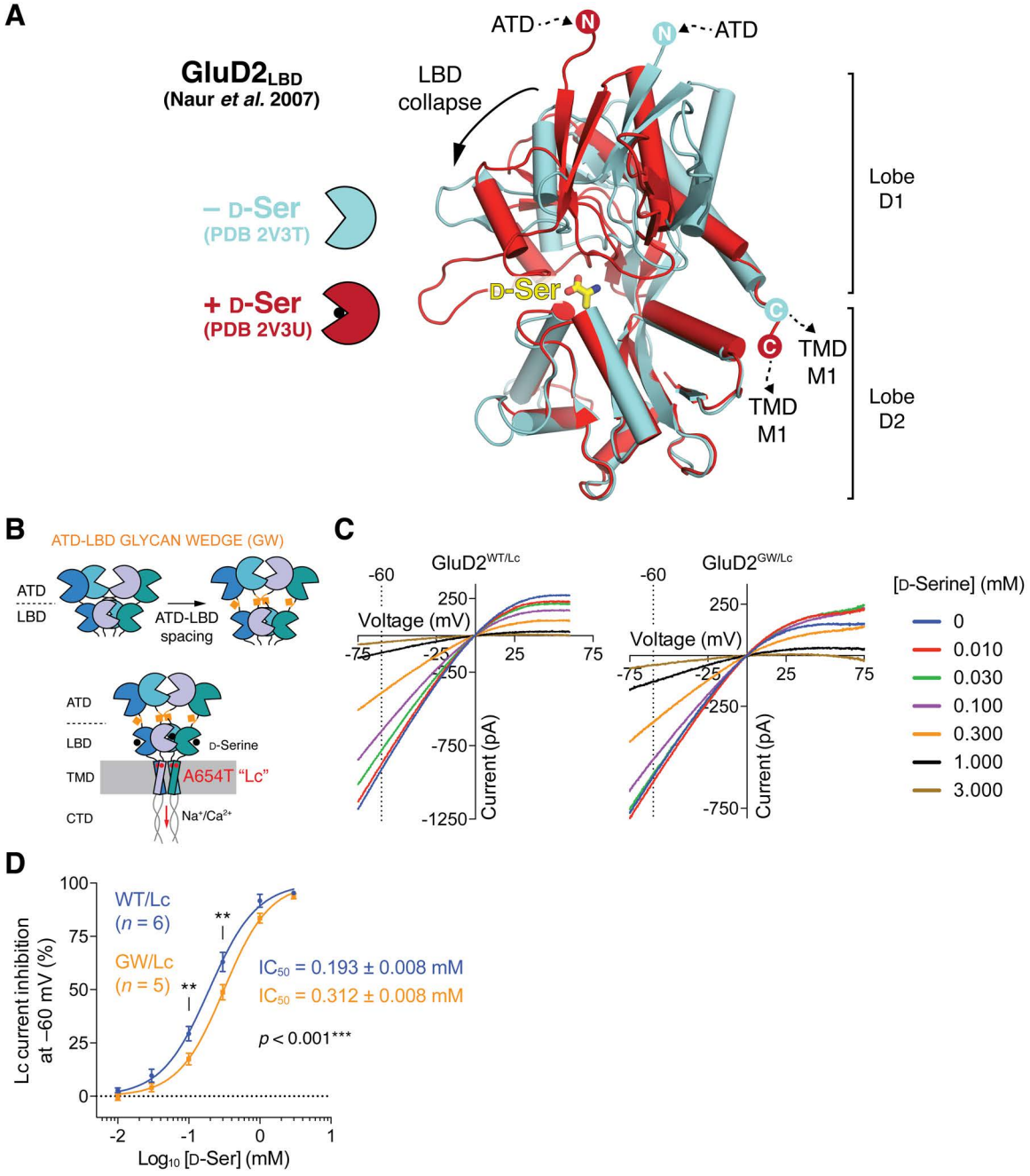

Fig. S18. Spacing of GluD2 ATD and LBD Layers Impacts on Agonist Binding.

(A) Structures of the GluD2 LBD in free (PDB code 2V3T (*33*)) and D-Ser-bound (PDB code 2V3U (*33*)) states, superposed using their D2 lobes. **(B)** Schematic representation of the GluD2$^{GW/Lc}$ construct. The position of the A654T "Lc" mutation in TMD helix segment M3 is indicated. **(C)** Current-Voltage (*I-V*) curves for GluD2$^{WT/Lc}$ and GluD2$^{GW/Lc}$, showing D-serine-induced inhibition of Lc currents. **(D)** Summary of Lc current inhibition (at –60 mV) by titration

of D-serine. The overall p value and p values for separate 0.1 and 0.3 mM D-serine concentration points were obtained using a Tukey's test for multiple comparisons. Dose-inhibition curves for GluD2$^{WT/Lc}$ and GluD2$^{GW/Lc}$ were calculated by sigmoidal curve fitting using Hill's equation and the IC_{50} values were obtained. **; $p < 0.01$.

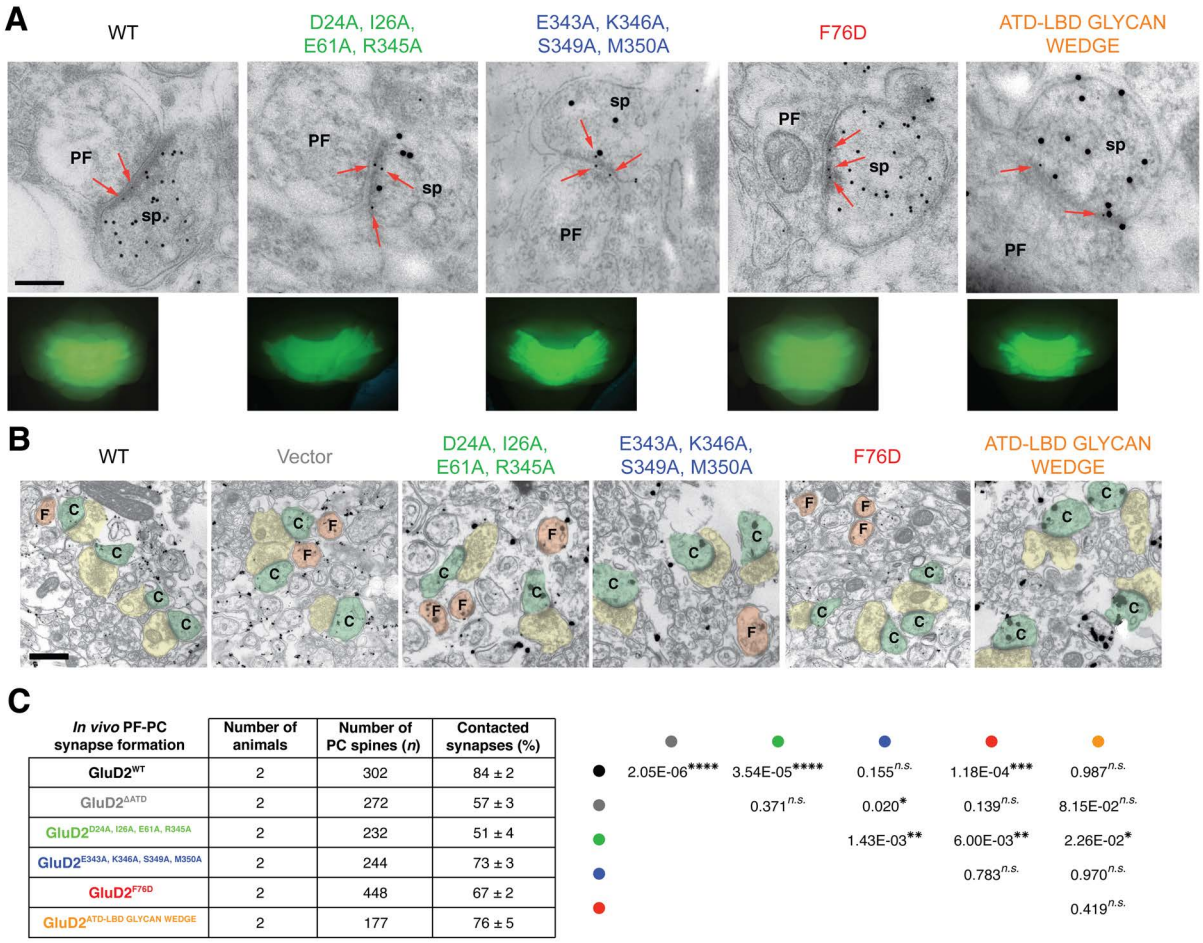

C

In vivo PF-PC synapse formation	Number of animals	Number of PC spines (*n*)	Contacted synapses (%)
GluD2^{WT}	2	302	84 ± 2
GluD2$^{\Delta ATD}$	2	272	57 ± 3
GluD2$^{D24A, I26A, E61A, R345A}$	2	232	51 ± 4
GluD2$^{E343A, K346A, S349A, M350A}$	2	244	73 ± 3
GluD2^{F76D}	2	448	67 ± 2
GluD2$^{ATD-LBD GLYCAN WEDGE}$	2	177	76 ± 5

2.05E-06****	3.54E-05****	0.155$^{n.s.}$	1.18E-04***	0.987$^{n.s.}$
	0.371$^{n.s.}$	0.020*	0.139$^{n.s.}$	8.15E-02$^{n.s.}$
		1.43E-03**	6.00E-03**	2.26E-02*
			0.783$^{n.s.}$	0.970$^{n.s.}$
				0.419$^{n.s.}$

Fig. S19. Structure-guided GluD2 Mutants Impact on PF-PC Synapse Formation *In Vivo*.

(A) Representative post-embedding immunogold EM images showing postsynaptic localization of GluD2^{WT}, GluD2$^{D24A, I26A, E61A, R345A}$, GluD2$^{E343A, K346A, S349A, M350A}$, GluD2^{F76D} and GluD2$^{ATD-LBD_GLYCAN_WEDGE}$ at *Grid2*-null (GluD2-deficient) PF-PC synapses. Arrows indicate GluD2-positive gold particles detected on the post-synaptic density (PSD). *sp*; PC spine. Scale bar; 200 nm. The insets show the cerebellum-wide GFP expression observed at 24 h after sub-arachnoidal injection of recombinant Sindbis virus. **(B)** Representative pre-embedding immunogold EM images showing synapses between PFs and PCs expressing wild-type GluD2 and structure-guided GluD2 mutants in *Grid2*-null cerebella. Labels "F" and "C" indicate free and contacted PC spines, respectively. Scale bar; 500 nm. **(C)** Summary of pre-embedding immunogold PF-PC synapse formation assay values and statistics. *p* values were obtained using a Kruskal-Wallis test followed by a Steel-Dwass test. ****; $p < 0.0001$, ***; $p < 0.001$, **; $p < 0.01$, *; $p < 0.05$, *n.s.*; not significant.

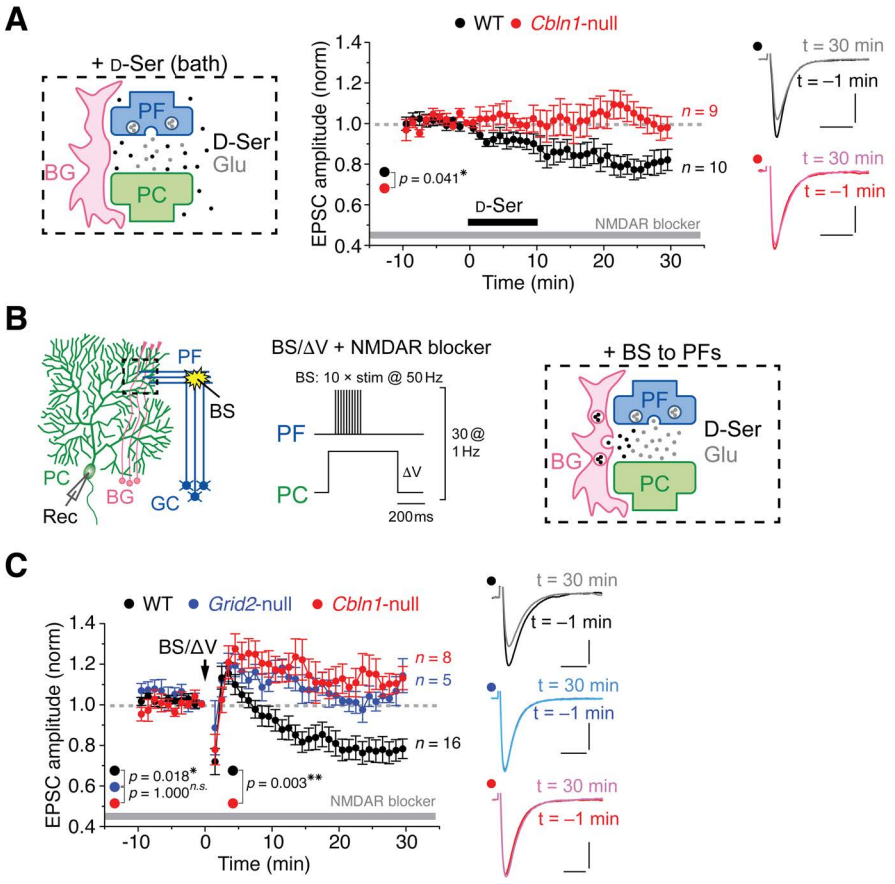

Fig. S20. LTD at PF-PC Synapses Requires Cbln1, GluD2 and D-serine.

(A) PF-EPSCs from mature wild-type and *Cbln1*-null PCs, induced by exogenous D-serine (D-Ser; 200 μM for 10 min). The insets show PF-EPSCs at t = –1 min and t = 30 min time points relative to D-Ser application. Data represent the mean ± SEM. *; $p < 0.05$ (Mann-Whitney U test). **(B)** Schematic representation of the experimental setup to induce LTD in immature PC dendrites. PC: Purkinje cell, GC: granule cell, PF: parallel fiber, BG: Bergmann glia, Rec: recording electrode. **(C)** Averaged LTD data from immature wild-type, *Grid2*-null (GluD2-deficient) and *Cbln1*-null PCs after burst PF stimulation (BS) combined with direct PC depolarization (ΔV) (BS/ΔV; arrow). The insets show PF-EPSCs at t = –1 min and t = 30 min time points relative to BS/ΔV application. Data represent the mean ± SEM. **; $p < 0.01$, *; $p < 0.05$, *n.s.*; not significant (Kruskal-Wallis and Steel-Dwass test). In (A-C), NMDA receptor blockers are 100 μM D-AP5 plus 25 μM MK801.

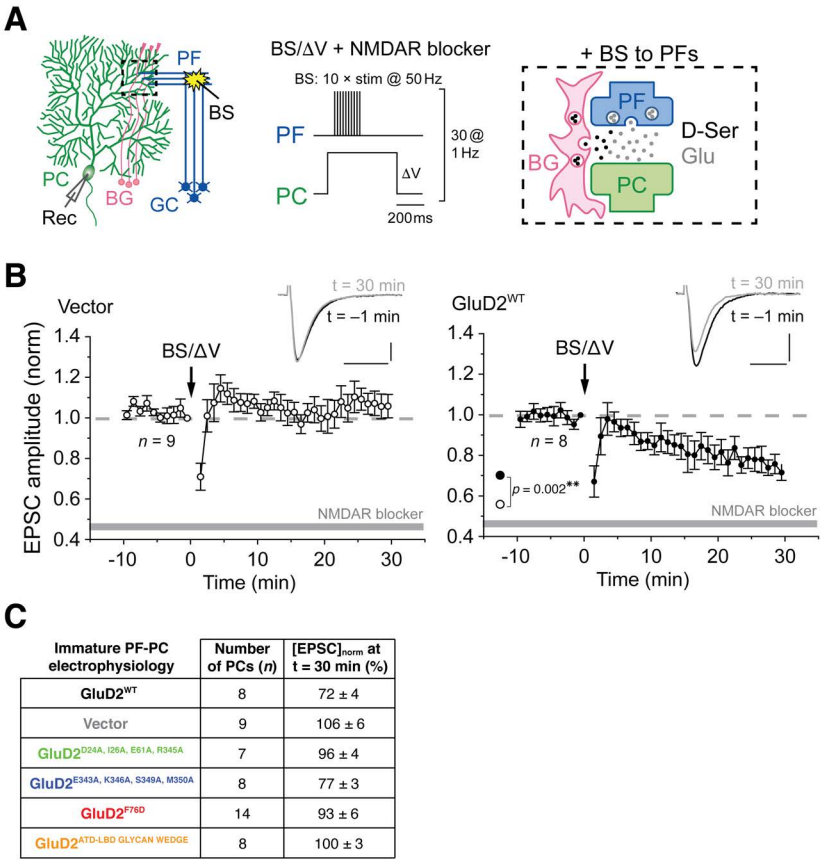

C

Immature PF-PC electrophysiology	Number of PCs (*n*)	$[EPSC]_{norm}$ at t = 30 min (%)
GluD2^{WT}	8	72 ± 4
Vector	9	106 ± 6
GluD2$^{D24A, I26A, E61A, R345A}$	7	96 ± 4
GluD2$^{E343A, K346A, S349A, M350A}$	8	77 ± 3
GluD2^{F76D}	14	93 ± 6
GluD2$^{ATD\text{-}LBD\ GLYCAN\ WEDGE}$	8	100 ± 3

Fig. S21. Structure-guided GluD2 Mutants Impact on Synaptic Plasticity in the Immature Cerebellum.

(A) Schematic representation of the experimental setup to induce LTD in immature PC dendrites. PC: Purkinje cell, GC: granule cell, PF: parallel fiber, BG: Bergmann glia, Rec: recording electrode. **(B)** Averaged LTD data from *Grid2*-null (GluD2-deficient) PCs, isolated from immature mice, expressing GFP only (Vector, open circles) or GFP + GluD2^{WT} (black), after burst PF stimulation (BS; 10 x PF stimuli at 50 Hz) combined with direct PC depolarization (ΔV) (BS/ΔV; arrow) 30 x at 1 Hz. NMDAR blockers: 100 μM D-AP5 plus 25 μM MK801. The traces in the inset show the PF-EPSCs just before (t = –1 min) or 30 min after (t = 30 min) BS/ΔV. Data represent the mean ± SEM. *p* values were obtained using a Kruskal-Wallis test followed by a Steel-Dwass test. **; $p < 0.01$. **(C)** Summary of immature PF-PC LTD values.

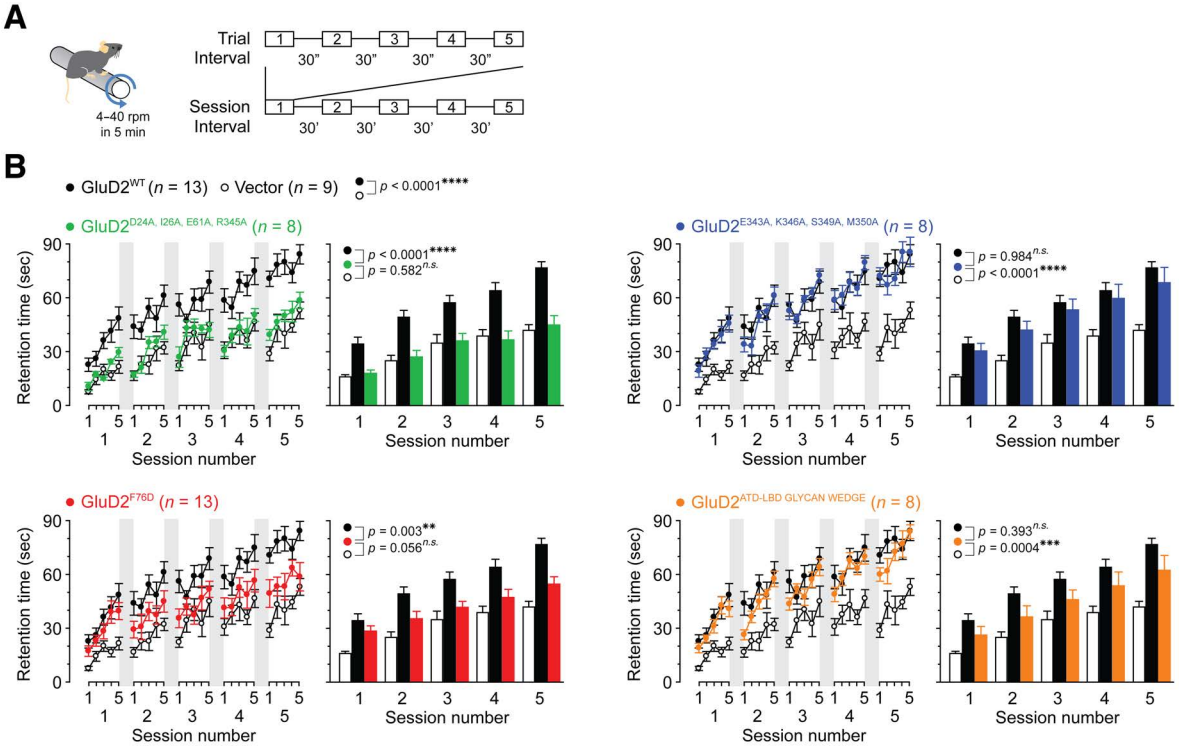

Fig. S22. Structure-guided GluD2 Mutants Impact on Gross Motor Coordination in Immature Mice.

(A) Schematic representation of the rotor-rod setup. **(B)** Rotor-rod test performance over the course of 5 trials (1 to 5) in immature *Grid2*-null mice expressing GFP only (Vector, open circles), GFP + GluD2^{WT} (black), GFP + GluD2$^{D24A,\ I26A,\ E61A,\ R345A}$ (green), GFP + GluD2$^{E343A,\ K346A,\ S349A,\ M350A}$ (blue), GFP + GluD2^{F76D} (red), and GFP + GluD2$^{ATD\text{-}LBD_GLYCAN_WEDGE}$ (orange). The right panels show averaged results for the 5 sessions of each trial. Data represent mean ± SEM. *p* values were obtained using a two-way repeated measure ANOVA. ****; $p < 0.0001$, ***; $p < 0.001$, **; $p < 0.01$, *n.s.*; not significant.

Supplementary Table 1 (Table S1). Crystallographic Data Collection and Refinement Statistics.

	$Cbln1_{C1q}$	**$Cbln1^{\Delta VRSG}$ crystal form 1 uncorrected**	**$Cbln1^{\Delta VRSG}$ crystal form 1 anisotropy-corrected**	**$Cbln1^{\Delta VRSG}$ crystal form 2**	**$GluD2_{ATD}$**	**$GluD1_{ATD}$**	**$Cbln1_{C1q}$–$GluD2_{ATD}$**
PDB code	5KC5	5KC6	5KC6	5KC7	5KC8	5KC9	5KCA
DATA COLLECTION							
Source	DLS I04	DLS I03	DLS I03	DLS I03	DLS I04	DLS I04-1	DLS I24
Wavelength λ (Å)	1.07300	0.97630	0.97630	0.97625	1.00000	0.91730	0.96862
No. of crystals	1	1	1	1	1	1	2
Resolution (Å)	50.57-2.35 (2.41-2.35)	85.22 – 2.80 (2.87-2.80)	85.22 – 2.80 (2.90-2.80)	76.55 – 7.00 (7.22-7.00)	57.03-1.75 (1.80-1.75)	59.22-2.30 (2.36-2.30)	46.05-3.10 (3.18-3.10)
Space group	*P*6	$C222_1$	$C222_1$	$I2_13$	*I*222	$P3_221$	$P6_122$
Metric Symmetry	*P*622						
Cell dimensions; a, b, c (Å)	83.42, 83.42, 50.57	79.58, 170.45, 116.43	79.58, 170.45, 116.43	187.52, 187.52, 187.52	45.10, 79.16, 246.69	128.42, 128.42, 153.23	142.68, 142.68, 276.14
Unique reflections	8497 (623)	19629 (1412)	14603 (370)	1801 (132)	44958 (3229)	65080 (4686)	30725 (2205)
Multiplicity	8.1 (8.1)	6.6 (6.3)	6.5 (6.1)	9.4 (9.9)	15.3 (9.5)	8.5 (8.7)	7.6 (7.5)
Completeness (%)	100.0 (100.0)	98.6 (96.8)	73.4 (19.0)	99.9 (100.0)	99.6 (98.3)	99.7 (98.5)	99.6 (99.8)
Wilson B ($Å^2$) (ML estimate)	40.9	77.9	54.6	404.4	25.6	57.3	66.4
R_{MERGE} (%)	12.6 (126.3)	6.8 (132.7)	5.6 (42.5)	4.8 (39.4)	7.8 (131.4)	5.1 (122.2)	22.4 (137.7)
R_{MEAS} (%)	13.5 (135.0)	7.4 (144.8)	6.1 (46.5)	5.1 (41.6)	8.0 (138.8)	5.4 (130.1)	24.1 (148.0)
R_{PIM} (%)	4.7 (47.3)	2.9 (57.3)	2.4 (18.5)	2.4 (18.3)	2.0 (44.2)	1.9 (43.9)	8.4 (51.8)
$CC_{1/2}$ (%)	99.8 (59.9)	99.9 (78.8)	99.9 (91.7)	99.8 (96.2)	100.0 (81.8)	100.0 (78.5)	98.6 (49.9)
CC* (%)	99.9 (86.6)	99.9 (93.9)	99.9 (97.8)	99.9 (99.0)	100.0 (94.9)	100.0 (93.8)	99.6 (81.6)
Average $I/\sigma(I)$	15.2 (1.8)	15.4 (1.5)	21.7 (5.6)	28.2 (5.9)	24.2 (2.2)	22.6 (1.9)	9.5 (1.5)
REFINEMENT							
Resolution (Å)	50.55-2.35 (2.69-2.35)		68.79-2.80 (3.02-2.80)	54.11-7.00	41.87-1.75 (1.80-1.75)	59.22-2.30 (2.33-2.30)	46.03-3.10 (3.20-3.10)
Reflections (Work / Free set)	8090 / 407		13853 / 708	1622 / 172	42689 / 2242	61798 / 3276	29171 / 1545
Twin Operator	*h, -h-k, -l*						
Twin fraction α	0.170						

R_{WORK} / R_{FREE} (%)	17.74 / 19.70 (25.30 / 29.61)		18.83 / 22.67 (23.87 / 22.20)	26.97 / 35.10	18.92 / 21.84 (30.46 / 34.20)	19.92 / 22.73 (29.76 / 33.97)	20.44 / 23.08 (32.82 / 39.05)
No. of atoms (protein/NAG/EDO/ PG4/BU1/calcium/chloride/ water)	1081 / 14 / 0 / 0 / 0 / 0 / 0 / 55		3326 / 42 / 0 / 0 / 0 / 0 / 0 / 0	4276 / 0 / 0 / 0 / 0 / 0 / 0 / 0	3143 / 0 / 12 / 0 / 0 / 2 / 0 / 237	9107 / 42 / 116 / 13 / 12 / 0 / 14 / 179	6331 / 0 / 0 / 0 / 0 / 1 / 0 / 0
B factors ($Å^2$) (protein/NAG/EDO/ PG4/BU1/calcium/chloride/ water)	44.7 / 85.4 / - / - / - / - / - / 46.9		58.8 / 86.6 / - / - / - / - / - / -	469.2 / - / - / - / - / - / - / -	41.3 / - / 65.2 / - / - / 44.4 / - / 43.7	77.8 / 104.1 / 81.1 / 65.8 / 65.0 / - / 97.5 / 59.6	62.9 / - / - / - / - / 90.3 / - / -
R.m.s.d. bonds (Å)	0.002		0.003	0.004	0.008	0.004	0.005
R.m.s.d. angles (°)	0.559		0.722	0.916	0.917	0.855	0.966
Ramachandran							
Favored (%)	95.56		98.06	97.74	97.72	97.10	94.72
Allowed (%)	4.44		1.94	2.26	2.28	2.72	4.65
Outliers (%)	0.00		0.00	0.00	0.00	0.18	0.63
Molprobity Score / percentile	1.36 / 100th		0.81 / 100th	1.65 / 100th	1.06 / 100th	1.25 / 100th	1.53 / 100th

Numbers in parentheses refer to the highest resolution shell.

R.m.s.d.: root mean square deviation from ideal geometry.

ML: maximum likelihood.

R_{SYM}: merging R-factor.

R_{PIM}: precision-indicating merging R-factor (*100*).

R_{MEAS}: multiplicity-corrected merging R-factor (*101*).

$CC_{1/2}$, CC*: correlation coefficients between random half data sets (*102, 103*).

NAG: N-Acetyl-D-Glucosamine.

EDO: Ethylene glycol.

PG4: Tetraethylene glycol.

BU1: *1,4*-Butanediol.

References and Notes

1. S. F. Traynelis, L. P. Wollmuth, C. J. McBain, F. S. Menniti, K. M. Vance, K. K. Ogden, K. B. Hansen, H. Yuan, S. J. Myers, R. Dingledine, Glutamate receptor ion channels: Structure, regulation, and function. *Pharmacol. Rev.* **62**, 405–496 (2010). Medline doi:10.1124/pr.109.002451

2. E. Karakas, H. Furukawa, Crystal structure of a heterotetrameric NMDA receptor ion channel. *Science* **344**, 992–997 (2014). Medline doi:10.1126/science.1251915

3. C. H. Lee, W. Lü, J. C. Michel, A. Goehring, J. Du, X. Song, E. Gouaux, NMDA receptor structures reveal subunit arrangement and pore architecture. *Nature* **511**, 191–197 (2014). Medline doi:10.1038/nature13548

4. T. Nakagawa, Y. Cheng, E. Ramm, M. Sheng, T. Walz, Structure and different conformational states of native AMPA receptor complexes. *Nature* **433**, 545–549 (2005). Medline doi:10.1038/nature03328

5. A. I. Sobolevsky, M. P. Rosconi, E. Gouaux, X-ray structure, symmetry and mechanism of an AMPA-subtype glutamate receptor. *Nature* **462**, 745–756 (2009). Medline doi:10.1038/nature08624

6. B. Herguedas, J. García-Nafría, O. Cais, R. Fernández-Leiro, J. Krieger, H. Ho, I. H. Greger, Structure and organization of heteromeric AMPA-type glutamate receptors. *Science* **352**, aad3873 (2016). Medline doi:10.1126/science.aad3873

7. W. Kakegawa, K. Kohda, M. Yuzaki, The delta2 'ionotropic' glutamate receptor functions as a non-ionotropic receptor to control cerebellar synaptic plasticity. *J. Physiol.* **584**, 89–96 (2007). Medline doi:10.1113/jphysiol.2007.141291

8. W. Kakegawa, Y. Miyoshi, K. Hamase, S. Matsuda, K. Matsuda, K. Kohda, K. Emi, J. Motohashi, R. Konno, K. Zaitsu, M. Yuzaki, D-serine regulates cerebellar LTD and motor coordination through the δ2 glutamate receptor. *Nat. Neurosci.* **14**, 603–611 (2011). Medline doi:10.1038/nn.2791

9. K. Kohda, W. Kakegawa, S. Matsuda, T. Yamamoto, H. Hirano, M. Yuzaki, The δ2 glutamate receptor gates long-term depression by coordinating interactions between two AMPA receptor phosphorylation sites. *Proc. Natl. Acad. Sci. U.S.A.* **110**, E948–E957 (2013). Medline doi:10.1073/pnas.1218380110

10. J. Aow, K. Dore, R. Malinow, Conformational signaling required for synaptic plasticity by the NMDA receptor complex. *Proc. Natl. Acad. Sci. U.S.A.* **112**, 14711–14716 (2015). Medline doi:10.1073/pnas.1520029112

11. K. Dore, J. Aow, R. Malinow, Agonist binding to the NMDA receptor drives movement of its cytoplasmic domain without ion flow. *Proc. Natl. Acad. Sci. U.S.A.* **112**, 14705–14710 (2015). Medline doi:10.1073/pnas.1520023112

12. N. L. Weilinger, A. W. Lohman, B. D. Rakai, E. M. Ma, J. Bialecki, V. Maslieieva, T. Rilea, M. V. Bandet, N. T. Ikuta, L. Scott, M. A. Colicos, G. C. Teskey, I. R. Winship, R. J. Thompson, Metabotropic NMDA receptor signaling couples Src family kinases to pannexin-1 during excitotoxicity. *Nat. Neurosci.* **19**, 432–442 (2016). Medline doi:10.1038/nn.4236

13. C. Auger, D. Ogden, AMPA receptor activation controls type I metabotropic glutamate receptor signalling via a tyrosine kinase at parallel fibre-Purkinje cell synapses. *J. Physiol.* **588**, 3063–3074 (2010). Medline doi:10.1113/jphysiol.2010.191080

14. T. Hayashi, H. Umemori, M. Mishina, T. Yamamoto, The AMPA receptor interacts with and signals through the protein tyrosine kinase Lyn. *Nature* **397**, 72–76 (1999). Medline doi:10.1038/16269

15. R. J. Rodrigues, J. Lerma, Metabotropic signaling by kainate receptors. *Wiley Interdiscip. Rev. Membr. Transp. Signal* **1**, 399–410 (2012). doi:10.1002/wmts.35

16. K. Matsuda, E. Miura, T. Miyazaki, W. Kakegawa, K. Emi, S. Narumi, Y. Fukazawa, A. Ito-Ishida, T. Kondo, R. Shigemoto, M. Watanabe, M. Yuzaki, Cbln1 is a ligand for an orphan glutamate receptor delta2, a bidirectional synapse organizer. *Science* **328**, 363–368 (2010). Medline doi:10.1126/science.1185152

17. G. M. Sia, J. C. Béïque, G. Rumbaugh, R. Cho, P. F. Worley, R. L. Huganir, Interaction of the N-terminal domain of the AMPA receptor GluR4 subunit with the neuronal pentraxin NP1 mediates GluR4 synaptic recruitment. *Neuron* **55**, 87–102 (2007). Medline doi:10.1016/j.neuron.2007.06.020

18. T. Uemura, S. J. Lee, M. Yasumura, T. Takeuchi, T. Yoshida, M. Ra, R. Taguchi, K. Sakimura, M. Mishina, Trans-synaptic interaction of GluRdelta2 and Neurexin through Cbln1 mediates synapse formation in the cerebellum. *Cell* **141**, 1068–1079 (2010). Medline doi:10.1016/j.cell.2010.04.035

19. L. Saglietti, C. Dequidt, K. Kamieniarz, M. C. Rousset, P. Valnegri, O. Thoumine, F. Beretta, L. Fagni, D. Choquet, C. Sala, M. Sheng, M. Passafaro, Extracellular interactions between GluR2 and N-cadherin in spine regulation. *Neuron* **54**, 461–477 (2007). Medline doi:10.1016/j.neuron.2007.04.012

20. K. Matsuda, T. Budisantoso, N. Mitakidis, Y. Sugaya, E. Miura, W. Kakegawa, M. Yamasaki, K. Konno, M. Uchigashima, M. Abe, I. Watanabe, M. Kano, M. Watanabe, K. Sakimura, A. R. Aricescu, M. Yuzaki, Transsynaptic Modulation of Kainate Receptor Functions by C1q-like Proteins. *Neuron* **90**, 752–767 (2016). Medline doi:10.1016/j.neuron.2016.04.001

21. H. Hirai, Z. Pang, D. Bao, T. Miyazaki, L. Li, E. Miura, J. Parris, Y. Rong, M. Watanabe, M. Yuzaki, J. I. Morgan, Cbln1 is essential for synaptic integrity and plasticity in the cerebellum. *Nat. Neurosci.* **8**, 1534–1541 (2005). Medline doi:10.1038/nn1576

22. K. Ryu, M. Yokoyama, M. Yamashita, T. Hirano, Induction of excitatory and inhibitory presynaptic differentiation by GluD1. *Biochem. Biophys. Res. Commun.* **417**, 157–161 (2012). Medline doi:10.1016/j.bbrc.2011.11.075

23. M. Yasumura, T. Yoshida, S. J. Lee, T. Uemura, J. Y. Joo, M. Mishina, Glutamate receptor δ1 induces preferentially inhibitory presynaptic differentiation of cortical neurons by interacting with neurexins through cerebellin precursor protein subtypes. *J. Neurochem.* **121**, 705–716 (2012). Medline doi:10.1111/j.1471-4159.2011.07631.x

24. Materials and methods are available as supplementary materials on Science Online.

25. Single-letter abbreviations for the amino acid residues are as follows: A, Ala; C, Cys; D, Asp; E, Glu; F, Phe; G, Gly; H, His; I, Ile; K, Lys; L, Leu; M, Met; N, Asn; P, Pro; Q, Gln; R, Arg; S, Ser; T, Thr; V, Val; W, Trp; and Y, Tyr.

26. D. Bao, Z. Pang, J. I. Morgan, The structure and proteolytic processing of Cbln1 complexes. *J. Neurochem.* **95**, 618–629 (2005). Medline doi:10.1111/j.1471-4159.2005.03385.x

27. J. R. Meyerson, J. Kumar, S. Chittori, P. Rao, J. Pierson, A. Bartesaghi, M. L. Mayer, S. Subramaniam, Structural mechanism of glutamate receptor activation and desensitization. *Nature* **514**, 328–334 (2014). Medline doi:10.1038/nature13603

28. A. Clayton, C. Siebold, R. J. Gilbert, G. C. Sutton, K. Harlos, R. A. McIlhinney, E. Y. Jones, A. R. Aricescu, Crystal structure of the GluR2 amino-terminal domain provides insights into the architecture and assembly of ionotropic glutamate receptors. *J. Mol. Biol.* **392**, 1125–1132 (2009). Medline doi:10.1016/j.jmb.2009.07.082

29. R. Jin, S. K. Singh, S. Gu, H. Furukawa, A. I. Sobolevsky, J. Zhou, Y. Jin, E. Gouaux, Crystal structure and association behaviour of the GluR2 amino-terminal domain. *EMBO J.* **28**, 1812–1823 (2009). Medline doi:10.1038/emboj.2009.140

30. J. Kumar, P. Schuck, R. Jin, M. L. Mayer, The N-terminal domain of GluR6-subtype glutamate receptor ion channels. *Nat. Struct. Mol. Biol.* **16**, 631–638 (2009). Medline doi:10.1038/nsmb.1613

31. J. Koehnke, P. S. Katsamba, G. Ahlsen, F. Bahna, J. Vendome, B. Honig, L. Shapiro, X. Jin, Splice form dependence of beta-neurexin/neuroligin binding interactions. *Neuron* **67**, 61–74 (2010). Medline doi:10.1016/j.neuron.2010.06.001

32. N. Kashiwabuchi, K. Ikeda, K. Araki, T. Hirano, K. Shibuki, C. Takayama, Y. Inoue, T. Kutsuwada, T. Yagi, Y. Kang, S. Aizawa, M. Mishina, Impairment of motor coordination, Purkinje cell synapse formation, and cerebellar long-term depression in GluR delta 2 mutant mice. *Cell* **81**, 245–252 (1995). Medline doi:10.1016/0092-8674(95)90334-8

33. P. Naur, K. B. Hansen, A. S. Kristensen, S. M. Dravid, D. S. Pickering, L. Olsen, B. Vestergaard, J. Egebjerg, M. Gajhede, S. F. Traynelis, J. S. Kastrup, Ionotropic

glutamate-like receptor delta2 binds D-serine and glycine. *Proc. Natl. Acad. Sci. U.S.A.* **104**, 14116–14121 (2007). Medline doi:10.1073/pnas.0703718104

34. M. Ito, K. Yamaguchi, S. Nagao, T. Yamazaki, Long-term depression as a model of cerebellar plasticity. *Prog. Brain Res.* **210**, 1–30 (2014). Medline doi:10.1016/B978-0-444-63356-9.00001-7

35. W. Kakegawa, T. Miyazaki, K. Emi, K. Matsuda, K. Kohda, J. Motohashi, M. Mishina, S. Kawahara, M. Watanabe, M. Yuzaki, Differential regulation of synaptic plasticity and cerebellar motor learning by the C-terminal PDZ-binding motif of GluRdelta2. *J. Neurosci.* **28**, 1460–1468 (2008). Medline doi:10.1523/JNEUROSCI.2553-07.2008

36. A. Ito-Ishida, T. Miyazaki, E. Miura, K. Matsuda, M. Watanabe, M. Yuzaki, S. Okabe, Presynaptically released Cbln1 induces dynamic axonal structural changes by interacting with GluD2 during cerebellar synapse formation. *Neuron* **76**, 549–564 (2012). Medline doi:10.1016/j.neuron.2012.07.027

37. K. L. Dürr, L. Chen, R. A. Stein, R. De Zorzi, I. M. Folea, T. Walz, H. S. Mchaourab, E. Gouaux, Structure and dynamics of AMPA receptor GluA2 in resting, pre-open, and desensitized states. *Cell* **158**, 778–792 (2014). Medline doi:10.1016/j.cell.2014.07.023

38. M. V. Yelshanskaya, M. Li, A. I. Sobolevsky, Structure of an agonist-bound ionotropic glutamate receptor. *Science* **345**, 1070–1074 (2014). Medline doi:10.1126/science.1256508

39. A. R. Aricescu, W. Lu, E. Y. Jones, A time- and cost-efficient system for high-level protein production in mammalian cells. *Acta Crystallogr. D Biol. Crystallogr.* **62**, 1243–1250 (2006). Medline doi:10.1107/S0907444906029799

40. V. T. Chang, M. Crispin, A. R. Aricescu, D. J. Harvey, J. E. Nettleship, J. A. Fennelly, C. Yu, K. S. Boles, E. J. Evans, D. I. Stuart, R. A. Dwek, E. Y. Jones, R. J. Owens, S. J. Davis, Glycoprotein structural genomics: Solving the glycosylation problem. *Structure* **15**, 267–273 (2007). Medline doi:10.1016/j.str.2007.01.011

41. P. J. Reeves, N. Callewaert, R. Contreras, H. G. Khorana, Structure and function in rhodopsin: High-level expression of rhodopsin with restricted and homogeneous N-glycosylation by a tetracycline-inducible N-acetylglucosaminyltransferase I-negative HEK293S stable mammalian cell line. *Proc. Natl. Acad. Sci. U.S.A.* **99**, 13419–13424 (2002). Medline doi:10.1073/pnas.212519299

42. Y. Zhao, B. Bishop, J. E. Clay, W. Lu, M. Jones, S. Daenke, C. Siebold, D. I. Stuart, E. Y. Jones, A. R. Aricescu, Automation of large scale transient protein expression in mammalian cells. *J. Struct. Biol.* **175**, 209–215 (2011). Medline doi:10.1016/j.jsb.2011.04.017

43. T. Kawate, E. Gouaux, Fluorescence-detection size-exclusion chromatography for precrystallization screening of integral membrane proteins. *Structure* **14**, 673–681 (2006). Medline doi:10.1016/j.str.2006.01.013

44. M. Hattori, R. E. Hibbs, E. Gouaux, A fluorescence-detection size-exclusion chromatography-based thermostability assay for membrane protein precrystallization screening. *Structure* **20**, 1293–1299 (2012). Medline doi:10.1016/j.str.2012.06.009

45. T. Nagai, K. Ibata, E. S. Park, M. Kubota, K. Mikoshiba, A. Miyawaki, A variant of yellow fluorescent protein with fast and efficient maturation for cell-biological applications. *Nat. Biotechnol.* **20**, 87–90 (2002). Medline doi:10.1038/nbt0102-87

46. R. S. Molday, D. MacKenzie, Monoclonal antibodies to rhodopsin: Characterization, cross-reactivity, and application as structural probes. *Biochemistry* **22**, 653–660 (1983). Medline doi:10.1021/bi00272a020

47. P. S. Miller, A. R. Aricescu, Crystal structure of a human GABAA receptor. *Nature* **512**, 270–275 (2014). Medline doi:10.1038/nature13293

48. K. L. Heckman, L. R. Pease, Gene splicing and mutagenesis by PCR-driven overlap extension. *Nat. Protoc.* **2**, 924–932 (2007). Medline doi:10.1038/nprot.2007.132

49. T. S. Walter, J. M. Diprose, C. J. Mayo, C. Siebold, M. G. Pickford, L. Carter, G. C. Sutton, N. S. Berrow, J. Brown, I. M. Berry, G. B. Stewart-Jones, J. M. Grimes, D. K. Stammers, R. M. Esnouf, E. Y. Jones, R. J. Owens, D. I. Stuart, K. Harlos, A procedure for setting up high-throughput nanolitre crystallization experiments. Crystallization workflow for initial screening, automated storage, imaging and optimization. *Acta Crystallogr. D Biol. Crystallogr.* **61**, 651–657 (2005). Medline doi:10.1107/S0907444905007808

50. O. Bogin, M. Kvansakul, E. Rom, J. Singer, A. Yayon, E. Hohenester, Insight into Schmid metaphyseal chondrodysplasia from the crystal structure of the collagen X NC1 domain trimer. *Structure* **10**, 165–173 (2002). Medline doi:10.1016/S0969-2126(02)00697-4

51. G. Winter, C. M. Lobley, S. M. Prince, Decision making in xia2. *Acta Crystallogr. D Biol. Crystallogr.* **69**, 1260–1273 (2013). Medline doi:10.1107/S0907444913015308

52. N. K. Sauter, R. W. Grosse-Kunstleve, P. D. Adams, Robust indexing for automatic data collection. *J. Appl. Crystallogr.* **37**, 399–409 (2004). Medline doi:10.1107/S0021889804005874

53. P. R. Evans, An introduction to data reduction: Space-group determination, scaling and intensity statistics. *Acta Crystallogr. D Biol. Crystallogr.* **67**, 282–292 (2011). Medline doi:10.1107/S090744491003982X

54. P. Evans, Scaling and assessment of data quality. *Acta Crystallogr. D Biol. Crystallogr.* **62**, 72–82 (2006). Medline doi:10.1107/S0907444905036693

55. W. Kabsch, Xds. *Acta Crystallogr. D Biol. Crystallogr.* **66**, 125–132 (2010). Medline doi:10.1107/S0907444909047337

56. A. J. McCoy, R. W. Grosse-Kunstleve, P. D. Adams, M. D. Winn, L. C. Storoni, R. J. Read, Phaser crystallographic software. *J. Appl. Crystallogr.* **40**, 658–674 (2007). Medline doi:10.1107/S0021889807021206

57. M. Strong, M. R. Sawaya, S. Wang, M. Phillips, D. Cascio, D. Eisenberg, Toward the structural genomics of complexes: Crystal structure of a PE/PPE protein complex from Mycobacterium tuberculosis. *Proc. Natl. Acad. Sci. U.S.A.* **103**, 8060–8065 (2006). Medline doi:10.1073/pnas.0602606103

58. P. D. Adams, P. V. Afonine, G. Bunkóczi, V. B. Chen, I. W. Davis, N. Echols, J. J. Headd, L. W. Hung, G. J. Kapral, R. W. Grosse-Kunstleve, A. J. McCoy, N. W. Moriarty, R. Oeffner, R. J. Read, D. C. Richardson, J. S. Richardson, T. C. Terwilliger, P. H. Zwart, PHENIX: A comprehensive Python-based system for macromolecular structure solution. *Acta Crystallogr. D Biol. Crystallogr.* **66**, 213–221 (2010). Medline doi:10.1107/S0907444909052925

59. G. N. Murshudov, P. Skubák, A. A. Lebedev, N. S. Pannu, R. A. Steiner, R. A. Nicholls, M. D. Winn, F. Long, A. A. Vagin, REFMAC5 for the refinement of macromolecular crystal structures. *Acta Crystallogr. D Biol. Crystallogr.* **67**, 355–367 (2011). Medline doi:10.1107/S0907444911001314

60. R. A. Nicholls, F. Long, G. N. Murshudov, Low-resolution refinement tools in REFMAC5. *Acta Crystallogr. D Biol. Crystallogr.* **68**, 404–417 (2012). Medline doi:10.1107/S090744491105606X

61. O. S. Smart, T. O. Womack, C. Flensburg, P. Keller, W. Paciorek, A. Sharff, C. Vonrhein, G. Bricogne, Exploiting structure similarity in refinement: Automated NCS and target-structure restraints in BUSTER. *Acta Crystallogr. D Biol. Crystallogr.* **68**, 368–380 (2012). Medline doi:10.1107/S0907444911056058

62. P. Emsley, B. Lohkamp, W. G. Scott, K. Cowtan, Features and development of Coot. *Acta Crystallogr. D Biol. Crystallogr.* **66**, 486–501 (2010). Medline doi:10.1107/S0907444910007493

63. V. B. Chen, W. B. Arendall 3rd, J. J. Headd, D. A. Keedy, R. M. Immormino, G. J. Kapral, L. W. Murray, J. S. Richardson, D. C. Richardson, MolProbity: All-atom structure validation for macromolecular crystallography. *Acta Crystallogr. D Biol. Crystallogr.* **66**, 12–21 (2010). Medline doi:10.1107/S0907444909042073

64. E. Krissinel, K. Henrick, Inference of macromolecular assemblies from crystalline state. *J. Mol. Biol.* **372**, 774–797 (2007). Medline doi:10.1016/j.jmb.2007.05.022

65. S. Loriot, F. Cazals, Modeling macro-molecular interfaces with Intervor. *Bioinformatics* **26**, 964–965 (2010). Medline doi:10.1093/bioinformatics/btq052

66. The PyMOL Molecular Graphics System, Version 1.7 (Schrödinger, LLC, 2015).

67. D. Eisenberg, E. Schwarz, M. Komaromy, R. Wall, Analysis of membrane and surface protein sequences with the hydrophobic moment plot. *J. Mol. Biol.* **179**, 125–142 (1984). Medline doi:10.1016/0022-2836(84)90309-7

68. D. I. Stuart, M. Levine, H. Muirhead, D. K. Stammers, Crystal structure of cat muscle pyruvate kinase at a resolution of 2.6 A. *J. Mol. Biol.* **134**, 109–142 (1979). Medline doi:10.1016/0022-2836(79)90416-9

69. C. S. Bond, A. W. Schüttelkopf, ALINE: A WYSIWYG protein-sequence alignment editor for publication-quality alignments. *Acta Crystallogr. D Biol. Crystallogr.* **65**, 510–512 (2009). Medline doi:10.1107/S0907444909007835

70. S. F. Altschul, W. Gish, W. Miller, E. W. Myers, D. J. Lipman, Basic local alignment search tool. *J. Mol. Biol.* **215**, 403–410 (1990). Medline doi:10.1016/S0022-2836(05)80360-2

71. R. C. Edgar, MUSCLE: Multiple sequence alignment with high accuracy and high throughput. *Nucleic Acids Res.* **32**, 1792–1797 (2004). Medline doi:10.1093/nar/gkh340

72. H. Ashkenazy, E. Erez, E. Martz, T. Pupko, N. Ben-Tal, ConSurf 2010: Calculating evolutionary conservation in sequence and structure of proteins and nucleic acids. *Nucleic Acids Res.* **38** (Web Server), W529–W533 (2010). Medline doi:10.1093/nar/gkq399

73. M. Ohi, Y. Li, Y. Cheng, T. Walz, Negative Staining and Image Classification - Powerful Tools in Modern Electron Microscopy. *Biol. Proced. Online* **6**, 23–34 (2004). Medline doi:10.1251/bpo70

74. J. Frank, M. Radermacher, P. Penczek, J. Zhu, Y. Li, M. Ladjadj, A. Leith, SPIDER and WEB: Processing and visualization of images in 3D electron microscopy and related fields. *J. Struct. Biol.* **116**, 190–199 (1996). Medline doi:10.1006/jsbi.1996.0030

75. M. Howarth, W. Liu, S. Puthenveetil, Y. Zheng, L. F. Marshall, M. M. Schmidt, K. D. Wittrup, M. G. Bawendi, A. Y. Ting, Monovalent, reduced-size quantum dots for imaging receptors on living cells. *Nat. Methods* **5**, 397–399 (2008). Medline doi:10.1038/nmeth.1206

76. D. G. Myszka, Improving biosensor analysis. *J. Mol. Recognit.* **12**, 279–284 (1999). Medline doi:10.1002/(SICI)1099-1352(199909/10)12:5<279::AID-JMR473>3.0.CO;2-3

77. P. Schuck, Size-distribution analysis of macromolecules by sedimentation velocity ultracentrifugation and lamm equation modeling. *Biophys. J.* **78**, 1606–1619 (2000). Medline doi:10.1016/S0006-3495(00)76713-0

78. W. Kakegawa, T. Miyazaki, K. Kohda, K. Matsuda, K. Emi, J. Motohashi, M. Watanabe, M. Yuzaki, The N-terminal domain of GluD2 (GluRdelta2) recruits presynaptic terminals

and regulates synaptogenesis in the cerebellum in vivo. *J. Neurosci.* **29**, 5738–5748 (2009). Medline doi:10.1523/JNEUROSCI.6013-08.2009

79. T. Takeuchi, T. Miyazaki, M. Watanabe, H. Mori, K. Sakimura, M. Mishina, Control of synaptic connection by glutamate receptor delta2 in the adult cerebellum. *J. Neurosci.* **25**, 2146–2156 (2005). Medline doi:10.1523/JNEUROSCI.4740-04.2005

80. K. Matsuda, M. Fletcher, Y. Kamiya, M. Yuzaki, Specific assembly with the NMDA receptor 3B subunit controls surface expression and calcium permeability of NMDA receptors. *J. Neurosci.* **23**, 10064–10073 (2003). Medline

81. E. Miura, T. Iijima, M. Yuzaki, M. Watanabe, Distinct expression of Cbln family mRNAs in developing and adult mouse brains. *Eur. J. Neurosci.* **24**, 750–760 (2006). Medline doi:10.1111/j.1460-9568.2006.04950.x

82. K. Kohda, W. Kakegawa, S. Matsuda, R. Nakagami, N. Kakiya, M. Yuzaki, The extreme C-terminus of GluRdelta2 is essential for induction of long-term depression in cerebellar slices. *Eur. J. Neurosci.* **25**, 1357–1362 (2007). Medline doi:10.1111/j.1460-9568.2007.05412.x

83. M. J. Schell, R. O. Brady Jr., M. E. Molliver, S. H. Snyder, D-serine as a neuromodulator: Regional and developmental localizations in rat brain glia resemble NMDA receptors. *J. Neurosci.* **17**, 1604–1615 (1997). Medline

84. K. Kohda, Y. Wang, M. Yuzaki, Mutation of a glutamate receptor motif reveals its role in gating and delta2 receptor channel properties. *Nat. Neurosci.* **3**, 315–322 (2000). Medline doi:10.1038/73877

85. F. Zheng, K. Erreger, C. M. Low, T. Banke, C. J. Lee, P. J. Conn, S. F. Traynelis, Allosteric interaction between the amino terminal domain and the ligand binding domain of NR2A. *Nat. Neurosci.* **4**, 894–901 (2001). Medline doi:10.1038/nn0901-894

86. M. Gielen, B. Siegler Retchless, L. Mony, J. W. Johnson, P. Paoletti, Mechanism of differential control of NMDA receptor activity by NR2 subunits. *Nature* **459**, 703–707 (2009). Medline doi:10.1038/nature07993

87. E. Karakas, N. Simorowski, H. Furukawa, Subunit arrangement and phenylethanolamine binding in GluN1/GluN2B NMDA receptors. *Nature* **475**, 249–253 (2011). Medline doi:10.1038/nature10180

88. S. J. Lee, T. Uemura, T. Yoshida, M. Mishina, GluRδ2 assembles four neurexins into trans-synaptic triad to trigger synapse formation. *J. Neurosci.* **32**, 4688–4701 (2012). Medline doi:10.1523/JNEUROSCI.5584-11.2012

89. X. Min, B. Lemon, J. Tang, Q. Liu, R. Zhang, N. Walker, Y. Li, Z. Wang, Crystal structure of a single-chain trimer of human adiponectin globular domain. *FEBS Lett.* **586**, 912–917 (2012). Medline doi:10.1016/j.febslet.2012.02.024

90. T. Kuroyanagi, T. Hirano, Flap loop of GluD2 binds to Cbln1 and induces presynaptic differentiation. *Biochem. Biophys. Res. Commun.* **398**, 537–541 (2010). Medline doi:10.1016/j.bbrc.2010.06.114

91. K. B. Hansen, P. Naur, N. L. Kurtkaya, A. S. Kristensen, M. Gajhede, J. S. Kastrup, S. F. Traynelis, Modulation of the dimer interface at ionotropic glutamate-like receptor delta2 by D-serine and extracellular calcium. *J. Neurosci.* **29**, 907–917 (2009). Medline doi:10.1523/JNEUROSCI.4081-08.2009

92. K. Konno, K. Matsuda, C. Nakamoto, M. Uchigashima, T. Miyazaki, M. Yamasaki, K. Sakimura, M. Yuzaki, M. Watanabe, Enriched expression of GluD1 in higher brain regions and its involvement in parallel fiber-interneuron synapse formation in the cerebellum. *J. Neurosci.* **34**, 7412–7424 (2014). Medline doi:10.1523/JNEUROSCI.0628-14.2014

93. R. Hepp, Y. A. Hay, C. Aguado, R. Lujan, L. Dauphinot, M. C. Potier, S. Nomura, O. Poirel, S. El Mestikawy, B. Lambolez, L. Tricoire, Glutamate receptors of the delta family are widely expressed in the adult brain. *Brain Struct. Funct.* **220**, 2797–2815 (2015). Medline doi:10.1007/s00429-014-0827-4

94. P. Wei, R. Pattarini, Y. Rong, H. Guo, P. K. Bansal, S. V. Kusnoor, A. Y. Deutch, J. Parris, J. I. Morgan, The Cbln family of proteins interact with multiple signaling pathways. *J. Neurochem.* **121**, 717–729 (2012). Medline doi:10.1111/j.1471-4159.2012.07648.x

95. K. Matsuda, M. Yuzaki, Cbln family proteins promote synapse formation by regulating distinct neurexin signaling pathways in various brain regions. *Eur. J. Neurosci.* **33**, 1447–1461 (2011). Medline doi:10.1111/j.1460-9568.2011.07638.x

96. T. Iijima, E. Miura, K. Matsuda, Y. Kamekawa, M. Watanabe, M. Yuzaki, Characterization of a transneuronal cytokine family Cbln—regulation of secretion by heteromeric assembly. *Eur. J. Neurosci.* **25**, 1049–1057 (2007). Medline doi:10.1111/j.1460-9568.2007.05361.x

97. W. Kakegawa, N. Mitakidis, E. Miura, M. Abe, K. Matsuda, Y. H. Takeo, K. Kohda, J. Motohashi, A. Takahashi, S. Nagao, S. Muramatsu, M. Watanabe, K. Sakimura, A. R. Aricescu, M. Yuzaki, Anterograde C1ql1 signaling is required in order to determine and maintain a single-winner climbing fiber in the mouse cerebellum. *Neuron* **85**, 316–329 (2015). Medline doi:10.1016/j.neuron.2014.12.020

98. J. Kumar, P. Schuck, M. L. Mayer, Structure and assembly mechanism for heteromeric kainate receptors. *Neuron* **71**, 319–331 (2011). Medline doi:10.1016/j.neuron.2011.05.038

99. M. Rossmann, M. Sukumaran, A. C. Penn, D. B. Veprintsev, M. M. Babu, I. H. Greger, Subunit-selective N-terminal domain associations organize the formation of AMPA receptor heteromers. *EMBO J.* **30**, 959–971 (2011). Medline doi:10.1038/emboj.2011.16

100. M. S. Weiss, R. Hilgenfeld, On the use of the merging R factor as a quality indicator for X-ray data. *J. Appl. Cryst.* **30**, 203–205 (1997). doi:10.1107/S0021889897003907

101. K. Diederichs, P. A. Karplus, Improved R-factors for diffraction data analysis in macromolecular crystallography. *Nat. Struct. Biol.* **4**, 269–275 (1997). Medline doi:10.1038/nsb0497-269

102. P. A. Karplus, K. Diederichs, Linking crystallographic model and data quality. *Science* **336**, 1030–1033 (2012). Medline doi:10.1126/science.1218231

103. P. R. Evans, G. N. Murshudov, How good are my data and what is the resolution? *Acta Crystallogr. D Biol. Crystallogr.* **69**, 1204–1214 (2013). Medline doi:10.1107/S0907444913000061